



Available online at www.sciencedirect.com

ScienceDirect

Comput. Methods Appl. Mech. Engrg. 347 (2019) 402–424

**Computer methods
in applied
mechanics and
engineering**

www.elsevier.com/locate/cma

A consistent spatially adaptive smoothed particle hydrodynamics method for fluid–structure interactions

Wei Hu^a, Guannan Guo^a, Xiaozhe Hu^b, Dan Negrut^a, Zhijie Xu^c, Wenxiao Pan^{a,*}

^a Department of Mechanical Engineering, University of Wisconsin-Madison, Madison, WI 53706, USA

^b Department of Mathematics, Tufts University, Medford, MA 02155, USA

^c Advanced Computing, Mathematics & Data Division, Pacific Northwest National Laboratory, Richland, WA 99352, USA

Received 5 March 2018; received in revised form 24 July 2018; accepted 15 October 2018

Available online 7 January 2019

Highlights

- A consistent, spatially adaptive smoothed particle hydrodynamics method is proposed for modeling fluid–structure interactions (FSI).
- The method allows for resolutions spatially adapted with moving (translating and rotating) boundaries of arbitrary geometries.
- It accelerates the FSI solution with significant savings in computational cost.
- It shows consistent accuracy and convergence.

Abstract

A new consistent, spatially adaptive, smoothed particle hydrodynamics (SPH) method for fluid–structure interactions (FSI) is presented. The method combines several attributes that have not been simultaneously satisfied by other SPH methods. Specifically, it employs the second-order consistent discretization for differential operators; it allows for resolutions spatially adapted with moving (translating and rotating) boundaries of arbitrary geometries; and, it accelerates the FSI solution as the adaptive approach leads to fewer degrees of freedom without sacrificing accuracy. The key ingredients in the method are a *posteriori* error estimator/distance-based criterion of adaptivity and a particle-shifting technique. The method is applied in simulating six different flows or FSI problems in two dimensions. The new method's convergence, accuracy, and efficiency attributes are assessed by comparing the results it produces with analytical, finite element, and consistent SPH uniform high-resolution solutions as well as experimental data.

© 2018 Elsevier B.V. All rights reserved.

Keywords: Spatially adaptive numerical methods; Meshless methods; Fluid–structure interactions; Smoothed particle hydrodynamics; Error estimator

1. Introduction

The FSI problem is encountered in a broad range of science and engineering applications, such as complex fluids [1–3], additive manufacturing [4–6], and carbon dioxide capture [7–9]. FSI problems are as ubiquitous as challenging.

* Corresponding author.

E-mail address: wpan9@wisc.edu (W. Pan).

Their solution must account for moving fluid–solid interfaces of complex geometries and hydrodynamic interactions between many immersed solid bodies. In this work, we propose a meshless particle method for solving FSI problems, which is based on a spatially adaptive, consistent SPH method. Different from the standard SPH method [10], in which the spatial discretization lacks consistency and hence results in less than second-order convergence that only can be recovered by taking increasingly large number of neighbors [11], the consistent SPH method ensures second-order consistency in its discretization of differential operators [11,12].

SPH solves partial differential equations (PDEs) numerically by approximating a variable at collocation points (or particles) throughout the domain via a smoothing function with a compact support (or smoothing length). As there is no assumed structure in the spatial distribution of the particles, they are completely *unstructured*. This unstructured nature allows for moving the particles with the dynamics of the problem and hence solving the underlying physics in a Lagrangian sense. As a result, there is no need to discretize the nonlinear advection term when solving the Navier–Stokes equation for fluid dynamics. Due to its meshless, Lagrangian nature, SPH has been widely applied in modeling multiphase flows with moving interfaces [13–15], complex fluids [16–19], materials subject to large deformation [20–22], FSI problems [23–25], and various transport phenomena [26–29].

In most SPH simulations, a uniform resolution is employed throughout the computational domain with SPH particles of uniform spacing and mass. This approach can be prohibitively expensive in modeling FSI problems when the near-field variables (velocity/pressure) surrounding solid bodies or within narrow gaps between solid boundaries must be accurately resolved. In such cases, the expectation is that resolving only a limited number of subdomains at high resolution while maintaining the rest of the simulation domain at lower particle resolution will yield efficiency gains without compromising the accuracy. This idea has been pursued in several multi-resolution or adaptive-resolution SPH methods [30–36].

In the multi-resolution scenario, the computational domain is pre-partitioned into a couple of subdomains. Each subdomain is discretized with SPH particles of a predefined spacing. What differentiates the methods in this scenario is how the subdomains of different resolutions are coupled, and how the predefined configuration of particle spacing is maintained as SPH particles advect with flow during the simulation. For example, in [34,35,37], each subdomain is assigned its own smoothing length according to its particle spacing. With the inconsistent SPH discretization, the accuracy and continuity of the numerical solution at and near the interface of subdomains is hard to maintain. The errors became notable as the ratio of the two resolutions increases [38]. To tackle this issue, a large, uniform smoothing length was used for all subdomains of different resolutions in [39]. This enhanced the accuracy attribute of the solution to some degree but led to a large number of neighbors for the particles in the high-resolution subdomain. Alternatively, an approach promoting different-resolution subdomains connected via an overlap region was proposed in [36]. The solutions in the two subdomains were synchronized at each time step via the overlap region where the state information and fluxes were exchanged by an iterative process. For the sake of numerical accuracy, a minimum thickness of the overlap region must be ensured and determined numerically. There are two concerns regarding this approach: (1) bringing the solutions of two subdomains in agreement via an iterative algorithm is costly and ad-hoc; and, (2) if the two subdomains are moving dynamically, continually establishing an adaptive overlap region is challenging. Against this backdrop, we proposed a different multi-resolution SPH method in [38]. Therein, each subdomain still has its own smoothing length, but the consistent discretization of differential operators was enforced via local correction matrices computed at each particle [11,40,41]. Without resorting to an overlap region, the continuity and second-order accuracy of the numerical solution were guaranteed. Owing to its higher-order accuracy, this multi-resolution SPH method required fewer number of particles to achieve the same accuracy and thereby led to further computational savings. As SPH particles advect with flow and move from one subdomain into the other, the predefined multi-resolution configuration was maintained via dynamically splitting or merging SPH particles. More specifically, a “big” particle was split into several “small” ones according to a certain geometric arrangement centered at the location of the big particle. Conversely, a group of small particles were merged into a big one at the center-of-mass of these small particles. This particle splitting/merging technique is similar to those used in literature [32–35,37,42–45].

The limitation of these multi-resolution methods is that spatial resolutions are not varied adaptively throughout the domain but are predefined for each subdomain. As shown in our previous work, the convergence of numerical solutions is affected by the ratio of resolutions in two adjacent subdomains[38]. To maintain the second-order convergence, this ratio must be less than 2. As a result, the computational savings associated with using multi-resolution methods are limited. Hence, a method with a continuously adaptive spatial resolution is more attractive. Efforts along this line have been attempted in the past. For instance, Oger et al. used adaptive smoothing lengths in the solution domain

according to the distances of fluid particles to the solid boundary, with larger smoothing lengths used for particles further away from the solid boundary [31]. By using spatially adaptive smoothing lengths, they were able to capture the transient dynamics of a wedge moving in water with reduced computational cost [31]. However, in this approach the smoothing lengths were only allowed to vary within a rather small range (less than 3% for any two adjacent layers) and did not change during the simulation after initially assigned. Alternatively, in [46–49], SPH particles with ellipsoidal smoothing kernels were used to discretize the computational domain. In two dimensional problems, the two major smoothing lengths of the ellipsoidal kernel were allowed to adaptively vary on different particles according to the local number density of SPH particles. Note that both the method in [31] and the ellipsoidal-kernel approach were based on the inconsistent SPH discretization, and their accuracy and convergence were not systematically assessed.

In this work, we propose a new, consistent adaptive-resolution SPH method for modeling FSI. In this method, spatial resolutions in the fluid domain are adaptively varied according to appropriate criteria of adaptivity. In particular, two criteria of adaptivity are assessed. The first one is distance-based – the spatial resolutions gradually vary according to the distances to the solid boundary. The second one draws on a *posteriori* error estimation. Note that in the literature of adaptive finite element methods (AFEM) for solving second-order elliptic PDEs, there are mainly two types of a *posteriori* error estimators. One is the residual-based error estimator [50,51]; the other one is the recovery-based error estimator [52,53]. Although a rigorous convergence theory for AFEM can be established based on the residual-based error estimator [51], we adopt the recovery-based error estimator for the SPH method for the following two reasons. First, the residual-based error estimator is derived from the variational formulation and, therefore, strongly depends on the problem being solved. The recovery-based error estimator is solely based on the computed solution and does not depend on the specific governing PDEs, which makes it more flexible and suitable for the SPH method compared with residual type error estimators. Second, although the theoretical justification of a recovery-based *posteriori* error estimator is still under investigation [54,55], in practice, it is usually more reliable and efficient compared with the residual-based error estimators; i.e., it provides more accurate estimations of the true errors [54,56].

Against this backdrop, our recovery-based *posteriori* error estimator for the SPH method borrows from its AFEM counterpart. It measures the difference between the direct and recovered velocity gradient [53]. In the AFEM, the recovered velocity gradient is determined by interpolation of the direct velocity gradients via the FE shape function. Motivated by that, the recovered velocity gradient in SPH is defined by interpolation of the direct velocity gradients via the SPH kernel function. With this error estimator evaluated at all SPH particles, following the error equidistribution strategy, the particles with larger or smaller errors are marked for refinement or coarsening. The masses of the particles marked for refinement or coarsening will be decreased or increased, respectively. A particle shifting technique is then employed to refine or coarsen particle spacings. Thus, a particle is shifted according to the shifting vector computed, and after shifting, hydrodynamic variables are corrected according to its new positions using a second-order interpolation. We note that this refinement/coarsening step is different from that used in the AFEM. Here, the total number and mass of particles do not change after refinement/coarsening. The two-way coupling of FSI is realized by imposing the no-slip boundary condition (BC) for the fluid at the solid boundary and moving the solid body with the force and torque exerted by the fluid. The forces and torques contributed by the pressure and viscous stress of the fluid are evaluated on the solid boundaries with the consistent discretization. The no-slip BC for the fluid velocity is imposed through ghost solid particles with velocities linearly extrapolated from the fluid velocity [57–60]. The proposed FSI method is validated and demonstrated to reduce computational costs without compromising accuracy. Compared with its mesh-based counterparts; i.e., AFEM and adaptive finite volume methods, the proposed SPH meshless solution for *moving* boundary FSI problems allows for adaptively varying spatial resolutions without the need of remeshing, a task that is generally expensive.

This paper is organized as follows. Section 2 describes the proposed consistent adaptive-resolution SPH method. Starting with a consistent SPH discretization, we explain next the approach for dynamically adapting spatial resolutions in solving the time-dependent problems. In Section 3, we demonstrate the accuracy, convergence, and efficiency of the proposed method through numerical tests. We model six different flows – the transient Poiseuille flow, flow around a periodic array of cylinders, flow around a cylinder in a narrow channel, two colloids rotating under a shear flow, dynamics of a low-symmetry active colloid, and collective dynamics of a suspension of active colloids – in two dimensions. The numerical results obtained are compared with analytical predictions, experimental data, and simulation results from the consistent uniform-resolution SPH or from other numerical methods such as FEM. Finally, we conclude and suggest directions of future work in Section 4.

2. Consistent adaptive-resolution SPH method

2.1. Governing equations

In FSI problems, the computational domain can be represented as $\Omega = \Omega_f \cup \Omega_s$, where Ω_f and Ω_s are the sub-domains occupied by the fluid and solid, respectively. The boundary Γ separates Ω_f and Ω_s , i.e., $\Gamma = \Omega_f \cap \Omega_s$.

2.1.1. Lagrangian hydrodynamics

The fluid velocity \mathbf{v} and pressure p are governed by the continuity and Naiver–Stokes (NS) equations:

$$\begin{cases} \frac{dp}{dt} = -\rho \nabla \cdot \mathbf{v} \\ \frac{d\mathbf{v}}{dt} = -\frac{\nabla p}{\rho} + \nu \nabla^2 \mathbf{v} + \mathbf{g} \quad \text{for } \mathbf{x} \in \Omega_f, \end{cases} \quad (1)$$

where \mathbf{g} denotes the body force per unit mass such as gravity; $\nu = \frac{\mu}{\rho}$ is the kinematic viscosity of the fluid; ρ and μ are the fluid density and viscosity, respectively. Here, the NS equations are written from a Lagrangian point of view with $d/dt = \partial/\partial t + \mathbf{v} \cdot \nabla$ denoting the total time derivative. Eq. (1) is closed by the equation of state (EOS):

$$p = c^2 \rho - p_0, \quad (2)$$

with a low Mach number (< 0.1) to approximately model an incompressible fluid. Here, $p_0 = c^2 \rho_0$, c is the speed of sound and ρ_0 is the initial density of the fluid [61–63].

2.1.2. Fluid–structure interactions

The fluid–solid coupling is modeled by imposing a no-slip BC for the fluid at the solid boundary; and, for the solid body, by accounting for the force and torque exerted by the fluid. The no-slip BC assumes the generic form $\mathbf{v}(\mathbf{x}) = \mathbf{v}_B(\mathbf{x})$; i.e., at any point of the boundary $\mathbf{x} \in \Gamma$, the velocity \mathbf{v} of the fluid and \mathbf{v}_B of the solid are identical. This condition should hold regardless whether the solid is rigid or deformable. For a rigid body, this condition can be further specified to read:

$$\mathbf{v} = \mathbf{v}_B = \mathbf{v}_d + \mathbf{r} \times \boldsymbol{\omega}_d \quad \text{for } \mathbf{x} \in \Gamma, \quad (3)$$

where \mathbf{v}_d and $\boldsymbol{\omega}_d$ denote the linear and angular velocities of the solid (rigid) body, respectively, and \mathbf{r} denotes the vector from the center-of-mass of the rigid body to the location $\mathbf{x} \in \Gamma$. Although the methodology presented here applies equally well to rigid and deformable bodies, the presentation continues with an assumption that the solid body is rigid (infinitely stiff). Its equations of motion are then governed by the differential equations:

$$\begin{cases} m_d \frac{d\mathbf{v}_d}{dt} = \mathbf{F}_d \\ I_d \frac{d\boldsymbol{\omega}_d}{dt} = \mathbf{T}_d, \end{cases} \quad (4)$$

where m_d and I_d represent the total mass and moment of inertia of the solid body, respectively. The total force \mathbf{F}_d and torque \mathbf{T}_d exerted on the solid body by fluid can be computed as:

$$\begin{cases} \mathbf{F}_d = \int_{\Gamma} \mathbf{n} \cdot \boldsymbol{\sigma} d\mathbf{x} \\ \mathbf{T}_d = \int_{\Gamma} \mathbf{r} \times (\mathbf{n} \cdot \boldsymbol{\sigma}) d\mathbf{x} \\ \boldsymbol{\sigma} = -p \mathbf{I} + \boldsymbol{\tau} \quad \text{with} \quad \boldsymbol{\tau} = \mu [\nabla \mathbf{v} + (\nabla \mathbf{v})^T], \end{cases} \quad (5)$$

where $\boldsymbol{\sigma}$ is the stress tensor; $\boldsymbol{\tau}$ is the viscous stress.

2.2. Spatial discretization

In SPH, the computational domain is discretized by a set of particles. The particles within Ω_f and Ω_s are referred to as “fluid” and “solid” particles, respectively. The value of a function f at a particle i is then approximated as [10]:

$$f_i = \sum_j f_j W_{ij} \mathcal{V}_j. \quad (6)$$

Here, \mathcal{V} is the volume of a SPH particle defined as $\mathcal{V}_i = (\sum_j W_{ij})^{-1}$. Hence, the mass of a SPH particle is given by $m_i = \rho_i \mathcal{V}_i$. In Eq. (6), $W_{ij} = W(\mathbf{r}_{ij})$ is the kernel function. In this work, we use the quintic spline function W that has continuous and smooth first and second derivatives:

$$W_{ij} = \alpha_d \begin{cases} (3 - R)^5 - 6(2 - R)^5 + 15(1 - R)^5 & 0 \leq R < 1 \\ (3 - R)^5 - 6(2 - R)^5 & 1 \leq R < 2 \\ (3 - R)^5 & 2 \leq R < 3 \\ 0 & R \geq 3. \end{cases} \quad (7)$$

In Eq. (7), the constant α_d assumes the value of $7/478\pi h^2$ for two-dimensional (2D) simulations; $R = \frac{r_{ij}}{h}$ with h denoting the kernel length and $r_{ij} = |\mathbf{r}_{ij}|$. Here, $\mathbf{r}_{ij} = \mathbf{x}_i - \mathbf{x}_j$ where \mathbf{x}_i is the position of particle i . For future reference, $\mathbf{e}_{ij} = \mathbf{r}_{ij}/r_{ij}$. With this kernel function, an SPH particle j contributes to the summation in Eq. (6) for approximating the function at particle i only when $j \in \mathcal{N}_{h,i} = \{\mathbf{x}_j : |\mathbf{x}_j - \mathbf{x}_i| < 3h\}$.

In the consistent SPH discretization [11,38,40,41], the gradient and Laplacian of the function f_i are discretized as:

$$\nabla f_i = \sum_j (f_j - f_i) (\mathbf{G}_i \cdot \nabla_i W_{ij}) \mathcal{V}_j, \quad (8)$$

$$\nabla^2 f_i = 2 \sum_j [\mathbf{L}_i : (\mathbf{e}_{ij} \otimes \nabla_i W_{ij})] \left(\frac{f_i - f_j}{r_{ij}} - \mathbf{e}_{ij} \cdot \nabla f_i \right) \mathcal{V}_j, \quad (9)$$

where “ \otimes ” represents the dyadic product of two vectors, and “ $:$ ” represents the double dot product of two matrices. Previous studies have demonstrated that this discretization of the gradient and Laplacian, which involves the symmetric correction matrices $\mathbf{G}_i, \mathbf{L}_i \in \mathbb{R}^{2 \times 2}$, guarantees the exact gradient for linear functions and Laplacian for parabolic functions regardless of the ratio of $h/\Delta x$ and hence displays second-order accuracy [11]. Here, Δx is the particle spacing. A detailed description of \mathbf{G}_i and \mathbf{L}_i can be found in [38]. For a vector function, the discretization in Eq. (8) is used for defining the discrete divergence operator. Hence, the consistent SPH discretization of the governing equations is given as:

$$\frac{d\rho_i}{dt} = -\rho_i \sum_j (\mathbf{v}_j - \mathbf{v}_i) \cdot (\mathbf{G}_i \cdot \nabla_i W_{ij}) \mathcal{V}_j, \quad (10)$$

$$\frac{d\mathbf{v}_i}{dt} = -\sum_j \frac{1}{\rho_j} (p_j - p_i) (\mathbf{G}_i \cdot \nabla_i W_{ij}) \mathcal{V}_j + 2 \sum_j v_j [\mathbf{L}_i : (\mathbf{e}_{ij} \otimes \nabla_i W_{ij})] \left(\frac{\mathbf{v}_i - \mathbf{v}_j}{r_{ij}} - \mathbf{e}_{ij} \cdot \nabla \mathbf{v}_i \right) \mathcal{V}_j + \mathbf{g}_i. \quad (11)$$

As noted, the consistent SPH discretization does not guarantee local conservation of momentum. As a result, the total force exerted by the fluid on the solid cannot be computed directly from the summation of forces contributed by the solid particles to fluid particles as in the conservative SPH methods [64]. Alternatively, we compute the force from the pressure and viscous stress evaluated on the solid boundary as in Eq. (5). To that end, we assign a new set of particles exactly on the boundary surface. Note that these “surface” particles do not participate in discretizing and solving the governing equations but only serve for evaluating the pressure and viscous stress exerted by the fluid on the solid boundary, from which the total force and torque on the solid are obtained. For evaluating the viscous stress, the gradient operator in $\boldsymbol{\tau} = \mu [\nabla \mathbf{v} + (\nabla \mathbf{v})^T]$ is discretized on the surface particles according to Eq. (8) with only fluid particles included in the summation as the neighbor particles. The pressure on the surface particles is calculated as [65]:

$$p_i = \frac{\sum_{j \in \text{fluid}} p_j W_{ij} + (\mathbf{g} - \mathbf{f}_i) \cdot \sum_{j \in \text{fluid}} \rho_j \mathbf{r}_{ij} W_{ij}}{\sum_{j \in \text{fluid}} W_{ij}}, \quad (12)$$

which considers the contribution of the net force acting on the solid from the body force (\mathbf{g}) of the fluid and acceleration (\mathbf{f}_i) of the surface particles. The latter is defined as:

$$\mathbf{f}_i = \frac{d\mathbf{v}_d}{dt} + \frac{d\boldsymbol{\omega}_d}{dt} \times \mathbf{r}_i + \boldsymbol{\omega}_d \times (\boldsymbol{\omega}_d \times \mathbf{r}_i) \quad (13)$$

Finally, the total force and torque applied on the immersed solid body can be evaluated by approximating Eq. (5) using the midpoint quadrature rule:

$$\mathbf{F}_d = \sum_{i \in \text{surface}} (\mathbf{n}_i \cdot \boldsymbol{\sigma}_i) \Delta S \quad \text{and} \quad \mathbf{T}_d = \sum_{i \in \text{surface}} \mathbf{r}_i \times (\mathbf{n}_i \cdot \boldsymbol{\sigma}_i) \Delta S, \quad (14)$$

where \mathbf{n}_i is the exterior normal vector at the position of surface particle i ; ΔS is the spacing between two neighbor surface particles; and \mathbf{r}_i denotes the vector from the center-of-mass of the solid body pointing to the surface particle i .

2.3. Imposition of the no-slip boundary condition

To accurately impose the no-slip boundary condition for the fluid velocity, the SPH approximations of velocity and its spatial derivatives for the fluid particles near the fluid–solid boundary must attain full support of the kernel contained in the domain ($\Omega_f \cup \Omega_s$). Thus, we follow the approach used in our previous work [38,41] and in literature [57,58,60] to lay several layers of ghost particles in the solid domain near the boundary. These ghost particles are assigned velocities linearly extrapolated from the velocities of fluid particles, i.e.,

$$\mathbf{v}_j = \frac{d_j}{d_i}(\mathbf{v}_B - \mathbf{v}_i) + \mathbf{v}_B , \quad (15)$$

where i is a fluid particle; j represents a solid ghost particle; d_i and d_j denote the closest perpendicular distances to the boundary for the fluid and ghost particles, respectively; and \mathbf{v}_B is the velocity of the solid boundary as in Eq. (3). This linear extrapolation introduces a local $\mathcal{O}(h^2)$ error [59] matching the second-order accuracy of the consistent SPH. In practice, d_i and d_j in Eq. (15) are approximated by [60]:

$$d_i = \omega h_i(2\chi_i - 1) , \quad d_j = \omega h_j(2\chi_j - 1) ,$$

with $\omega = 3$ for the quintic spline function used herein. The indicator χ used to differentiate fluid and solid particles is given as:

$$\chi_i = \frac{\sum_{k \in \text{fluid}} W_{ik}}{\sum_k W_{ik}} , \quad \chi_j = \frac{\sum_{k \in \text{solid}} W_{jk}}{\sum_k W_{jk}} .$$

2.4. Time integration

The variables defined on fluid particles are updated via a standard second-order, explicit predictor–corrector scheme [38,66,67]. In the predictor step, the intermediate velocity $\bar{\mathbf{v}}_i$ and position $\bar{\mathbf{x}}_i$ at the intermediate time step $(t + \frac{\Delta t}{2})$ are first predicted as:

$$\begin{cases} \bar{\mathbf{v}}_i(t + \frac{\Delta t}{2}) = \mathbf{v}_i(t) + \frac{\Delta t}{2} \mathbf{a}_i(t) \\ \bar{\mathbf{x}}_i(t + \frac{\Delta t}{2}) = \mathbf{x}_i(t) + \frac{\Delta t}{2} \mathbf{v}_i(t) , \end{cases}$$

where $\mathbf{a}_i = \frac{d\mathbf{v}_i}{dt}$ is the total acceleration of particle i determined from Eq. (11). The intermediate density $\bar{\rho}_i(t + \frac{\Delta t}{2})$ and pressure $\bar{p}_i(t + \frac{\Delta t}{2})$ are then obtained via Eqs. (2) and (10), respectively. After the predictor step, $\mathbf{a}_i(t + \frac{\Delta t}{2})$ is evaluated and subsequently used in the corrector step:

$$\begin{cases} \mathbf{v}_i(t + \frac{\Delta t}{2}) = \mathbf{v}_i(t) + \frac{\Delta t}{2} \mathbf{a}_i(t + \frac{\Delta t}{2}) \\ \mathbf{x}_i(t + \frac{\Delta t}{2}) = \mathbf{x}_i(t) + \frac{\Delta t}{2} \mathbf{v}_i(t + \frac{\Delta t}{2}) . \end{cases}$$

Finally, the particle's velocity and position at $t + \Delta t$ are updated by:

$$\begin{cases} \mathbf{v}_i(t + \Delta t) = 2\mathbf{v}_i(t + \frac{\Delta t}{2}) - \mathbf{v}_i(t) \\ \mathbf{x}_i(t + \Delta t) = 2\mathbf{x}_i(t + \frac{\Delta t}{2}) - \mathbf{x}_i(t) , \end{cases}$$

while the density $\rho_i(t + \Delta t)$ and pressure $p_i(t + \Delta t)$ are obtained via Eqs. (2) and (10), respectively. In this predictor–corrector scheme, the time step Δt is constrained by the CFL condition [68], magnitude of acceleration $|\mathbf{a}_i|$, and viscous dispersion as:

$$\Delta t \leq \min\{0.25 \frac{h}{c}, 0.25 \min_i (\frac{h}{|\mathbf{a}_i|})^{\frac{1}{2}}, 0.125 \frac{h^2}{v}\} .$$

For the solid body, the velocity \mathbf{v}_d , angular velocity $\boldsymbol{\omega}_d$, angle θ_d and position \mathbf{x}_d at the intermediate time step are first computed from:

$$\begin{cases} \mathbf{v}_d(t + \frac{\Delta t}{2}) = \mathbf{v}_d(t) + \frac{\Delta t}{2} \frac{\mathbf{F}_d(t)}{m_d} \\ \mathbf{x}_d(t + \frac{\Delta t}{2}) = \mathbf{x}_d(t) + \frac{\Delta t}{2} \mathbf{v}_d(t) \\ \boldsymbol{\omega}_d(t + \frac{\Delta t}{2}) = \boldsymbol{\omega}_d(t) + \frac{\Delta t}{2} \frac{\mathbf{T}_d(t)}{I_d} \\ \theta_d(t + \frac{\Delta t}{2}) = \theta_d(t) + \frac{\Delta t}{2} \boldsymbol{\omega}_d(t). \end{cases}$$

With this information at the intermediate time step, $\mathbf{F}_d(t + \frac{\Delta t}{2})$ and $\mathbf{T}_d(t + \frac{\Delta t}{2})$ are evaluated and used to update the variables of the next time step as:

$$\begin{cases} \mathbf{v}_d(t + \Delta t) = \mathbf{v}_d(t) + \Delta t \frac{\mathbf{F}_d(t + \frac{\Delta t}{2})}{m_d} \\ \mathbf{x}_d(t + \Delta t) = \mathbf{x}_d(t) + \Delta t \mathbf{v}_d(t + \frac{\Delta t}{2}) \\ \boldsymbol{\omega}_d(t + \Delta t) = \boldsymbol{\omega}_d(t) + \Delta t \frac{\mathbf{T}_d(t + \frac{\Delta t}{2})}{I_d} \\ \theta_d(t + \Delta t) = \theta_d(t) + \Delta t \boldsymbol{\omega}_d(t + \frac{\Delta t}{2}). \end{cases}$$

2.5. Approach for adapting spatial resolutions

In the present work, we assessed two spatial-resolution adaptivity criteria. The first one is distance-based, and it varies the spatial resolution in the fluid domain gradually according to distances to the solid boundary. The second one is based on an error estimator, namely, the recovery-based *a posteriori* error estimator.

2.5.1. Recovery-based error estimator

The recovery-based error estimator measures the difference between the direct and recovered velocity gradient in the energy norm [53] and has been commonly used in the adaptive FEM [55,56]. In the framework of consistent SPH, this error estimator can be evaluated locally on each fluid particle i at every timestep as:

$$\|\mathbf{e}_i\|^2 = m_i \|(\mathbf{R}[\mathbf{v}]_i - \nabla \mathbf{v}_i)\|^2. \quad (16)$$

Here, $\mathbf{R}[\mathbf{v}]_i$ represents the recovered velocity gradient

$$\mathbf{R}[\mathbf{v}]_i = \sum_j (\nabla \mathbf{v}_j) W_{ij} \mathcal{V}_j, \quad (17)$$

where $\nabla \mathbf{v}_i$ is the local velocity gradient evaluated in the discrete setting using Eq. (8). The energy norm $\|\cdot\|^2$ in Eq. (16) is defined as the element-wise inner product, i.e., $\|\mathbf{e}\|^2 = \mathbf{e} : \mathbf{e} = e^{mn} e^{mn}$, where the Einstein summation convention is adopted.

2.5.2. Adaptive algorithm

Initially, the SPH particles are distributed with a uniform resolution (spacing) Δx_{ini} and mass m_0 . During the simulation, the initial spacing is dynamically adapted to new distributions of variable resolution. In this process, the total number of SPH particles (N_{tot}) and, therefore, the total degree of freedom (DOF) count, do not change. Before the procedure starts, we preset the finest resolution $\Delta x_H = \Delta x_{ini}/\lambda$ allowed in the simulation domain, where λ is the ratio of the initial particle spacing to the particle spacing of the finest resolution allowed and can be any positive real number larger than 1. Given that, the mass of the smallest particle is $m_H = m_0/\lambda^D$, where D is the dimension of the simulation domain. With the total number and mass of SPH particles conserved, the mass of the largest particle is set as $m_L = (2\lambda^D - 1)m_0/\lambda^D$. The maximum resolution ratio Υ_{max} is defined as the ratio of the coarsest resolution (Δx_L) to the finest resolution (Δx_H) throughout the simulation domain, i.e., $\Upsilon_{max} = \Delta x_L/\Delta x_H$. With the masses of largest and smallest particles determined, we obtain $\Upsilon_{max} = (2\lambda^D - 1)^{\frac{1}{D}}$. Thus, if a smaller Δx_H is chosen, Δx_L and Υ_{max} are larger. Given the simulation domain is finite, a larger Υ_{max} results in larger ratios of resolutions of any two adjacent SPH particles. Here, we choose Δx_H or λ such that the maximum ratio of resolutions of any two adjacent SPH particles is less than 2. Otherwise, according to our previous study [38], the convergence of the solution could worsen.

At the end of each time step, after all variables have been updated following the schemes described in Sections 2.2–2.4 based on the current spatial resolutions, a three-step process is carried out to adjust the spatial resolutions as follows:

ESTIMATE → MARK → REFINE/COARSEN.

In the **ESTIMATE** step, depending on which criterion is employed; i.e., error-based or distance-based, we first calculate for each fluid particle either its recovered error of the velocity gradient, or its distance to specified solid boundaries.

1. If the *error-based* criterion is employed:

The MARK step: The local error estimated via Eq. (16) in the ESTIMATE step will indicate which particles are relatively too large or too small in the current particle spatial distribution. These particles are then MARK-ed for refining or coarsening. Following the error equidistribution strategy, particles with larger or smaller errors are potentially candidates for refinement or coarsening. More specifically, the top 5% of particles with the largest errors will be refined if their current resolutions have not reached the preset Δx_H ; and, the bottom 5% of particles with the smallest errors will be coarsened if their resolutions have not reached the predetermined Δx_L . The 5%-value is conservative enough to ensure the numerical stability. More than 5% can result in non-smooth particle distributions near the solid boundary, which in turn would lead to unstable simulations. Fewer than 5% would cause more iterations required to meet the preset tolerance (in Eq. (22)). In each time step, the total number of particles marked for refinement is equal to that marked for coarsening such that conservation of the total mass can be enforced. If the mass of some particle reaches the maximum or minimum mass, this particle will not be marked for refinement/coarsening. Also, the total mass is tracked to ensure it constant during the simulation.

The REFINE/COARSEN step: The refinement for the error-based criterion is realized by reducing the mass of a SPH particle m_i by Δm ; and, the coarsening is enforced by increasing m_i by Δm . In our study, we found that the simulation is more stable when $\Delta m = 0.1\%m_0$. For the particle whose mass is changed, its smoothing length h_i must be changed proportionally to the new mass assigned, i.e., by the factor of $(\frac{m_i \pm \Delta m}{m_i})^{\frac{1}{D}}$.

2. If the *distance-based* criterion is employed:

The MARK step: The fluid particles are sorted according to their distances to specified solid boundaries calculated in the ESTIMATE step and all MARK-ed for refining or coarsening. As the distance of each fluid particle to the solid boundary does not change much between two continuous time steps, the refining/coarsening needed is reasonably small.

The REFINE/COARSEN step: According to the sorting of distances to the solid boundary, all fluid particles are assigned new masses and kernel lengths. In a technique that renders the mass of particles closer to the solid boundary smaller, the refining starts with a step in which we preset the number of smallest particles (N_m) needed to resolve the subdomain near the solid boundary. With the total number and mass of SPH particles conserved, we next solve for an integer N_m that best approximates the nonlinear equation:

$$N_H m_H + (N_{tot} - N_H - N_m) m_L + \sum_{i=1}^{N_m} m_H \left(\frac{m_L}{m_H} \right)^{\frac{i}{N_m+1}} = N_{tot} m_0. \quad (18)$$

With N_m in hand, $(N_{tot} - N_H - N_m)$ represents the number of largest particles; and, N_m particles have the masses between m_L and m_H ; i.e., $m_i^{new} = m_H \left(\frac{m_L}{m_H} \right)^{\frac{i}{N_m+1}}$ with $i = 1, 2, \dots, N_m$. Finally, the particles' smoothing lengths are updated proportionally to the new masses assigned, i.e., by the factor of $(\frac{m_i^{new}}{m_i})^{\frac{1}{D}}$.

After the new masses and smoothing lengths of fluid particles are determined in the REFINE/COARSEN step, the distribution of particles is adapted using a particle-shifting technique. To this end, a shifting vector $\delta \mathbf{r}_i$ is first defined as:

$$\delta \mathbf{r}_i = \frac{\beta r_0^2 \Delta x_{ini} h_i}{\bar{m}_i h_{ini}} \sum_j m_j \frac{\mathbf{r}_{ij}}{r_{ij}^3}, \quad (19)$$

where $r_0 = \frac{1}{N_i} \sum_j r_{ij}$; $N_i = |\mathcal{N}_{h,i}|$; $\bar{m}_i = \sum_j m_j$; and β is an adjustable dimensionless parameter and set as $\beta = 0.05$ in this work. The particle-shifting technique was originally proposed in [69] for preventing clustering and voids in the

distribution of SPH particles with uniform resolutions. We have made modifications by adding particle mass m and kernel length h , as shown in Eq. (19), to make it applicable for adapting the distribution of SPH particles to achieve adaptive resolutions. With this shifting vector, the position of particle i is then updated as:

$$\mathbf{x}_i^{new} = \mathbf{x}_i + \delta \mathbf{r}_i. \quad (20)$$

Based on its new position, each particle receives a small velocity and density correction via a second-order interpolation:

$$\psi_i^{new} = \psi_i + \nabla \psi_i \cdot \delta \mathbf{r}_i, \quad (21)$$

where the field variable ψ_i represents \mathbf{v}_i or ρ_i , and $\nabla \psi_i$ is calculated according to Eq. (8). The second-order accuracy of this interpolation scheme matches that of the consistent SPH discretization. For consistency, the pressure p_i^{new} is also corrected using ρ_i^{new} via the EOS (Eq. (2)). After the particle positions are shifted, the REFINE/COARSEN step concludes. A new distribution of variable resolutions is generated for the solution at the next time step. We note that in the generated new distribution of variable resolutions, the total number and mass of SPH particles stay unchanged, which is different from the REFINE/COARSEN step implemented in the AFEM.

The proposed adaptive algorithm has three salient attributes. First, the adaptive-resolution implementation does not pose any additional constraints on Δt . Therefore, the computational efficiency gained only depends on the number of particles saved and the overhead involved in the adaptive algorithm.

Second, this three-step procedure can be iterated for multiple times to attain an optimal distribution of adaptive resolutions. In the error-based criterion, we set a tolerance for the total relative error and terminate the iterations once the error satisfies:

$$\frac{\sum_i \|\mathbf{e}_i\|^2}{\sum_i m_i \|\nabla \mathbf{v}_i\|^2} \leq TOL, \quad (22)$$

where TOL is the preset tolerance, and $TOL = 0.02$ is used in this study. Through our numerical tests, we found that by and large one iteration per time step is sufficient to achieve the desired accuracy and savings of computational cost.

Third, starting with a uniform resolution might not be optimal in terms of accuracy and efficiency, especially when transient dynamics is to be captured in simulating FSI with freely moving solid bodies. Starting with a uniform resolution takes much more iterations for adapting resolutions in each time step especially during the early time steps. As a result, the particle positions are shifted significantly across the streamlines, adversely impacting the accuracy of the solution. Therefore, we prefer to “prime” these simulations with a preprocessing step, in which the solid body is fixed at its initial position, and the fluid particles are adapted following the adaptive algorithm described above using the distance-based criterion. The adaptive process iterates until a desired distribution of variable resolutions is attained, in which the shifting vectors computed from Eq. (19) in a new iteration are considerably small; i.e., $\frac{1}{\beta N_{tot}} \sum_i \frac{|\delta \mathbf{r}_i|}{(m_i/\rho_i)^{\frac{1}{D}}}$ is less than a preset threshold. Provided this “primed” particle distribution, we commence the actual dynamic simulation. The three-step adaptive algorithm (error-based or distance-based) is subsequently applied at the end of each time step, yet the number of iterations and the magnitudes of the shifting vectors are greatly reduced. This “prime-before-you-start” approach improves both the accuracy and efficiency of the numerical solution.

3. Simulation results

Six different problems were studied to assess the accuracy, convergence, and efficiency of the proposed consistent adaptive-resolution SPH method. In this exercise, the numerical results were compared with analytical solutions, experimental data, or numerical solutions obtained using either the FEM or consistent SPH method with uniform, high resolutions. Unless otherwise specified, in all simulations the fluid had $\rho = 10^3 \text{ kg/m}^3$ and kinetic viscosity $\nu = 10^{-4} \text{ m}^2/\text{s}$.

3.1. Transient Poiseuille flow

First, we considered the transient Poiseuille flow in a straight channel with two fixed walls oriented along the x axis and positioned at $y = 0 \text{ m}$ and $y = 0.1454 \text{ m}$. The flow was driven by a body force ($|\mathbf{g}| = 2 \times 10^{-4} \text{ m/s}^2$) acting along the x axis and subject to no-slip BCs at the two walls and periodic BCs at the remaining boundaries.

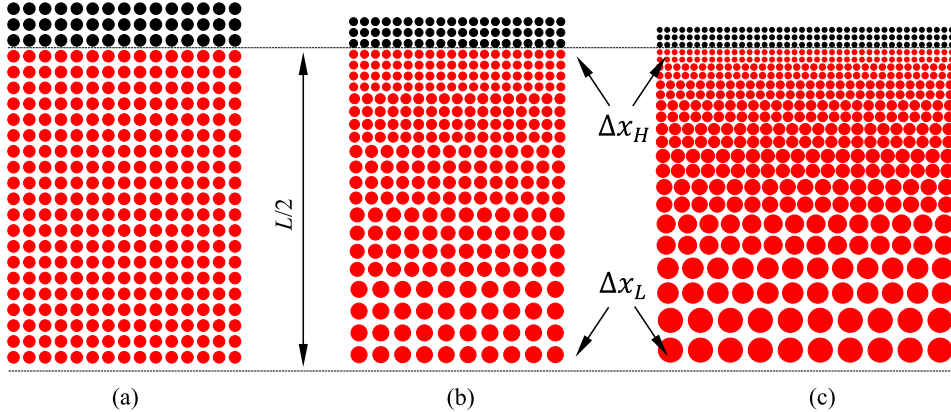


Fig. 1. Initial distribution of SPH particles with uniform/variable resolutions for modeling the transient Poiseuille flow. Due to the symmetry, only half of the simulation domain is shown. (a) Uniform resolution with $\Upsilon_{max} = 1$; (b) adaptive resolution with $\Upsilon_{max} = 2$; and, (c) adaptive resolution with $\Upsilon_{max} = 4$.

To assess the convergence of the adaptive-resolution numerical solution, we examined two different prescribed configurations of variable resolution. As shown in Fig. 1, the simulation domain was discretized by 5 or 10 different resolutions across the channel width with $\Upsilon_{max} = 2$ or 4, respectively. In either case, the ratio of any two adjacent resolutions is less than 1.33. The coarsest resolution (Δx_L) is near the center of the channel; the finest resolution (Δx_H) is near the channel walls.

For each of the three cases considered; i.e., $\Upsilon_{max} = 1$, 2, and 4, we assessed the convergence of the SPH solutions by varying the number of particles and monitoring the errors. We report L_2 error by comparing the numerically predicted steady-state velocity with the analytical solution. The results are presented in Fig. 2. First, the second-order convergence of the consistent adaptive-resolution SPH method can be obtained at all Υ_{max} values. Second, with the same number of particles across the channel width, larger Υ_{max} leads to smaller errors and hence higher accuracy, which implies that using variable resolution reduces the number of particles (or degrees of freedom) required to achieve a desired accuracy.

3.2. Flow around a periodic array of fixed cylinders

In this test, a cylinder of radius 0.02 m was positioned at the center of a square domain of length 0.1 m. The flow was driven by a body force $|\mathbf{g}| = 5 \times 10^{-5} \text{ m/s}^2$ along the x coordinate and subject to the no-slip BC at the surface of the cylinder and periodic BCs at the remaining boundaries. We adapted the spatial resolutions dynamically using the recovery-based error estimator computed at each time step. Initially, the SPH particles were distributed with a uniform resolution $\Delta x_{ini} = 1.25 \text{ mm}$. We prescribed the finest and coarsest spacing of particles in the adapted resolutions as $\Delta x_H = \frac{1}{4} \Delta x_{ini}$ and $\Delta x_L = \frac{\sqrt{31}}{4} \Delta x_{ini}$, respectively; i.e., $\Upsilon_{max} = \sqrt{31}$. The steps followed to adjust the resolution are as described in Section 2.5.2. Fig. 3 shows the distribution of adaptive resolutions at the steady state. (The transient dynamics is shown by the animation in the Supporting Information.)

To examine the accuracy of this numerical solution, the velocities along two vertical imaginary lines at $x = 0.05 \text{ m}$ (line 1) and at $x = 0.1 \text{ m}$ (line 2) were compared with those predicted by FEM with a higher, uniform resolution of $\Delta x = 0.25 \text{ mm} < \Delta x_H$. As shown in Fig. 4, the SPH solutions agree well with the FEM solutions. The FEM is second-order accurate and uses piecewise linear finite elements for discretization. We also compared the total drag force exerted on the cylinder by the fluid. The difference of our solution relative to that predicted by FEM is less than 1%. These results confirm the accuracy of the proposed method in modeling this flow.

In addition to accuracy, we examined the computational efficiency of the adaptive-resolution SPH in modeling this flow. To that end, we also conducted an SPH simulation using the uniform, high resolution Δx_H . This led to a number of particles 16 times higher than that used in the adaptive-resolution simulation. For both simulations, the time step was set as $6.25 \times 10^{-4} \text{ s}$. For each time step, the computational time is 0.89 s for adaptive resolution and 7.2 s for uniform-resolution. The uniform-resolution computational cost (in terms of computational time) was about 8 times

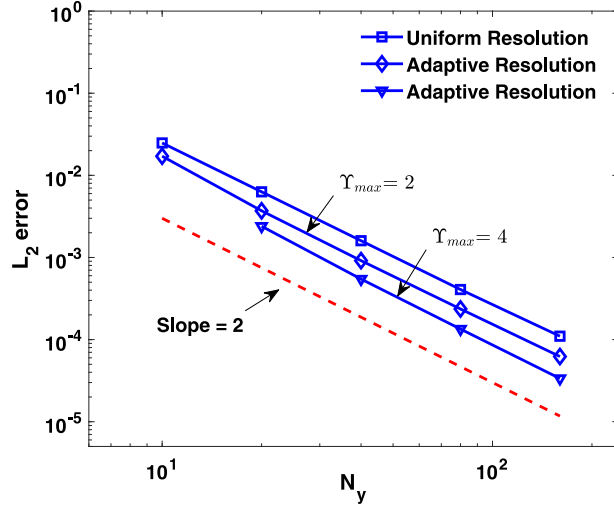


Fig. 2. Convergence of the numerical solutions on the steady-state velocity in Poiseuille flow for different γ_{max} . The x axis displays the number of particles across the channel width; the y axis is the L_2 error relative to the analytical solution.

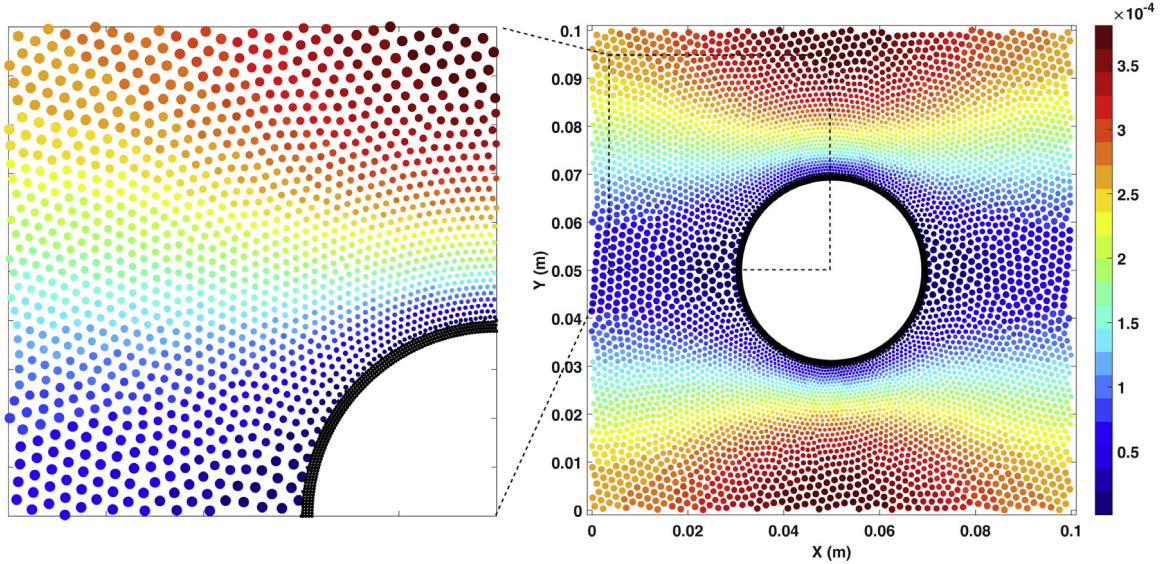


Fig. 3. Distribution of SPH particles in the flow around a fixed cylinder at steady state with the resolutions adapted according to the recovery-based error estimator. The color is correlated to the flow velocity magnitude (unit in the color bar: m/s). (For interpretation of the references to color in this figure legend, the reader is referred to the web version of this article.)

that of the adaptive-resolution simulation. By using the adaptive-resolution technique in this test, we saved about 93% degrees of freedom and 87% computer time without sacrificing accuracy.

3.3. Flow around a cylinder in a narrow channel

In this and the next tests, we simulated flows through narrow gaps between solid boundaries. The solid boundaries are either stationary or moving. The adaptive-resolution technique allowed for resolving the narrow gaps with sufficient resolutions but without increasing the total degrees of freedom of the simulations.

First, we consider a flow around a cylinder in a narrow channel. Fig. 5 describes the setup of this problem. The computational domain was a box of length $L = 0.3$ m and width $2H = 0.1$ m. A cylinder was at the center of the

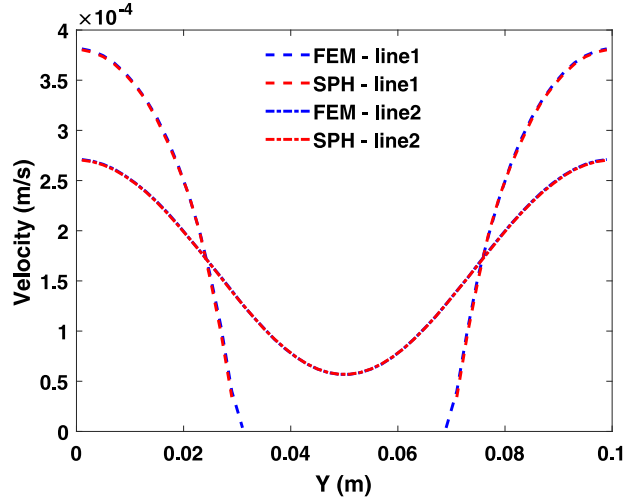


Fig. 4. The steady-state velocity profiles along lines 1 ($x = 0.05$ m) and 2 ($x = 0.1$ m), computed by the consistent adaptive-resolution SPH with $\Delta x_H = 0.3125$ mm and $\Upsilon_{max} = \sqrt{31}$ and FEM with a uniform resolution $\Delta x = 0.25$ mm.

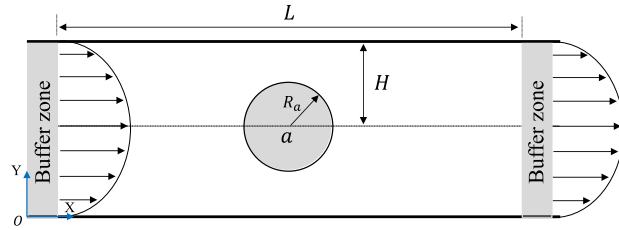


Fig. 5. Configuration of the flow around a cylinder centered in a channel. Here, $L = 0.3$ m; $2H = 0.1$ m; and, R_a varies from $0.1H$ to $0.9H$. Two buffer zones of ghost particles with a length of 0.02 m are set next to the inlet and outlet boundaries, respectively.

channel with the radius varied from $R_a = 0.1H$ to $R_a = 0.9H$. The larger the cylinder, the narrower the gap between the cylinder and channel walls. At the channel walls and surface of the cylinder, the flow was subject to no-slip BCs. To impose the prescribed inflow and outflow velocities at the inlet and outlet of the channel, two buffer zones of length 0.02 m were attached at the two ends. Particles in these buffer zones served as ghost particles for enforcing the Dirichlet boundary condition. The prescribed velocities were from the analytical solution of the steady-state Poiseuille flow. When particles moved out of the channel with flow, periodic boundary conditions were enforced.

SPH particles were initially distributed with a uniform spacing $\Delta x_{ini} = 2$ mm. For the cylinder of $R_a = 0.9H$, this resolution led to only 2 particles within the gap between the cylinder boundary and channel walls. For the kernel length used in the SPH discretization, at least 5 particles across the gap are needed to guarantee an accurate solution of the flow. However, this level of resolution throughout the simulation domain calls for prohibitively expansive simulations. Therefore, we maintained sufficiently fine resolutions within the gap but coarser resolutions for the remaining domain. Similarly to the previous case, we adapted the spatial resolutions according to the error estimator. We chose the finest resolution $\Delta x_H = \frac{1}{2}\Delta x_{ini}$ and the coarsest resolution $\Delta x_L = \frac{\sqrt{7}}{2}\Delta x_{ini}$, which gives $\Upsilon_{max} = \sqrt{7}$. Fig. 6 shows the distribution of adaptive resolutions at steady state. We note that the recovery-based error of velocity gradient effectively guided the redistribution of particles to the desired variable resolutions.

We monitored the drag force exerted on the cylinder as well as the pressure drop through the channel and compared them with analytical solutions, see Fig. 7(a). As the cylinder radius ($\frac{R_a}{2\rho v V_r}$) increases, the total drag force ($\frac{F}{2\rho v V_r}$) exerted on the cylinder grows rapidly and so does the pressure drop ($\frac{\Delta P_H}{\rho v V_r}$) of the flow, where V_r is the mean velocity of the prescribed Poiseuille flow. Both the drag and pressure drop solutions agree well with their analytical counterparts. To further assess the solution accuracy, we conducted an additional set of simulations, from which we computed the drift velocity of the cylinder driven by the flow. Following the work by Jeong and

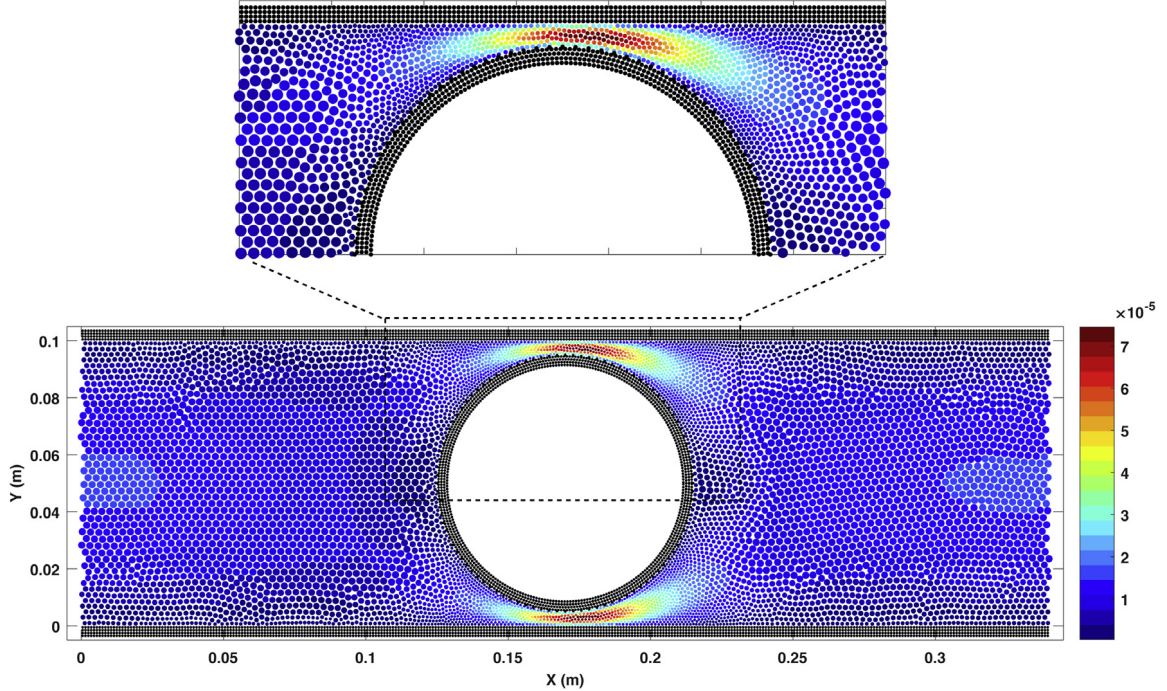


Fig. 6. Distribution of SPH particles in the flow around a cylinder in a narrow channel at the steady state with the resolutions adapted according to the recovery-based error computed during the simulation. The color is correlated to the flow velocity magnitude (unit in the color bar: m/s). (For interpretation of the references to color in this figure legend, the reader is referred to the web version of this article.)

Yoon [70], in this set of simulations the flow was set static initially, but the cylinder was moving at constant velocity equal to V_r . Again, we computed the drag force exerted on the cylinder by the fluid. The non-dimensional drift velocity ($\frac{V_c}{V_r}$) can be determined by the ratio of the drag force computed from the previous set of simulations to the drag force computed from this set of simulations [70]. Fig. 7(b) compares the non-dimensional drift velocity thus obtained with the analytical solution [70], and again, a good agreement is found. We hence demonstrated the accuracy of the proposed adaptive-resolution SPH method in simulating a flow with narrow gaps between solid boundaries. Further, we examined the convergence of the numerical solution for the drift velocity with $R_a/H = 0.5$ and found the first-order convergence rate, as shown in Fig. 8. The less than second-order convergence obtained is due to the following reasons. First, in this case, the pressure force significantly contributed in the total force on the cylinder. In this work, the weakly compressible equation of state was employed to approximate incompressibility and to solve for the pressure. This approximation is not numerically consistent. Next, the formulation in Eq. (12) used for evaluating the pressure force exerted on the cylinder is not compatible with the consistent discretization. Therefore, even though the second-order consistent discretization of differential operators was employed, the inconsistent approximation of the pressure diminished the numerical accuracy herein.

3.4. Dynamics of two cylinders under a shear flow

Next, we simulated the dynamics of two cylinders immersed in fluid subject to a plane shear flow. Fig. 9 illustrates the setup of this problem. The radius of the equal-sized cylinders is $R_a = R_b = 0.01$ m. Periodic BCs were applied at $x = 0$ and $x = 0.4$ m, and the solid walls were placed at $y = 0$ and $y = 0.4$ m with the no-slip BC. Thus, the size of the simulation domain is $L = H = 0.4$ m, which is large enough to neglect the effects of walls and periodic images of cylinders. To generate a plane shear flow with the shear rate of $\dot{\gamma} = \frac{2V_x}{H} = 1.25 \times 10^{-3}$ /s, the upper and lower walls were assigned velocities in opposite directions but with the same magnitude of $V_x = 2.5 \times 10^{-4}$ m/s. In this case, the kinetic viscosity of the fluid was assumed as $\nu = 10^{-5}$ m²/s. With that, the Reynolds number defined

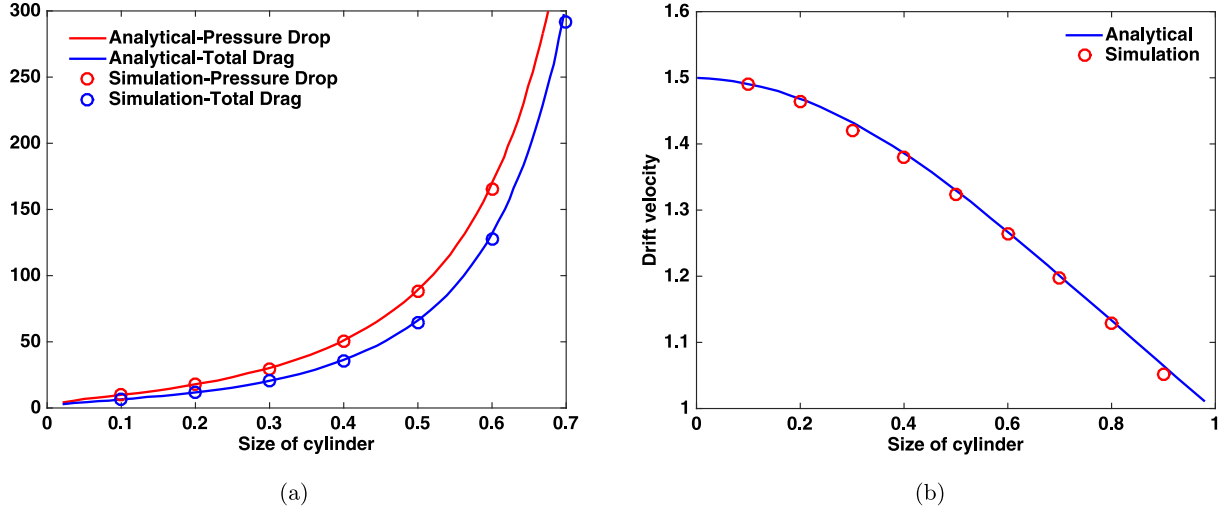


Fig. 7. (a) The total drag force exerted on the cylinder and pressure drop of the flow. (b) The non-dimensional drift velocity of the cylinder. Data are collected for different sizes of the cylinder (defined as R_a/H). Numerical results are compared with the analytical solutions [70].

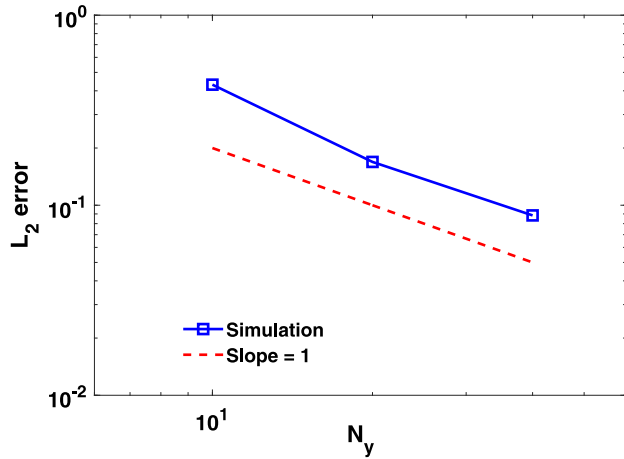


Fig. 8. Convergence of the numerical solution for the drift velocity with $R_a/H = 0.5$. The x axis displays the number of particles across the channel width; the y axis is the L_2 error relative to the analytical solution..

as $Re = \frac{\dot{\gamma} R_a^2}{\nu}$ has the same value as that in the literature [64,71,72], i.e., $Re = 0.0125$. Following the flow, the two cylinders rotated while approaching each other or moving apart.

In literature, this problem was previously solved both analytically [71] and numerically [64,72]. Varying the initial positions of the two cylinders, the translational trajectories of either cylinder's center of mass can be different. Following [64,72], we also considered three different initial positions of the cylinders. Correspondingly, the initial separations of the two cylinders in (x, y) were: (0.03 m, 0.02 m), (0.03 m, 0.012 m), and (0.024 m, 0.0 m), respectively.

In this problem, the fluid occupies most of the domain and is subject to shear flow with a constant shear rate. As a result, the recovery-based errors of velocity gradient showed very little difference across the entire domain. Thus, the error-based adaptive criterion was not effective here. Alternatively, we used the distance to the surfaces of the two cylinders as the criterion for adapting the spatial resolutions in this test in which we attempted to capture transient dynamics of freely moving cylinders. As discussed in Section 2.5.2, starting the simulation with a uniform resolution was not optimal in terms of accuracy and efficiency of the solution. Instead, we carried out a preprocessing step before the simulation. Therein, the two cylinders were fixed at their initial positions and the spatial resolution was adapted to

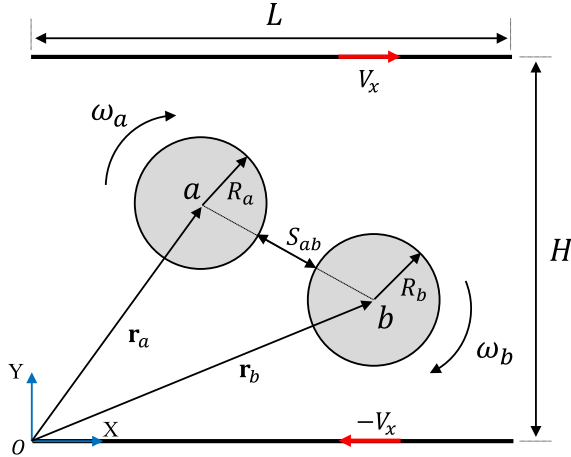


Fig. 9. Configuration of two cylinders under a shear flow.

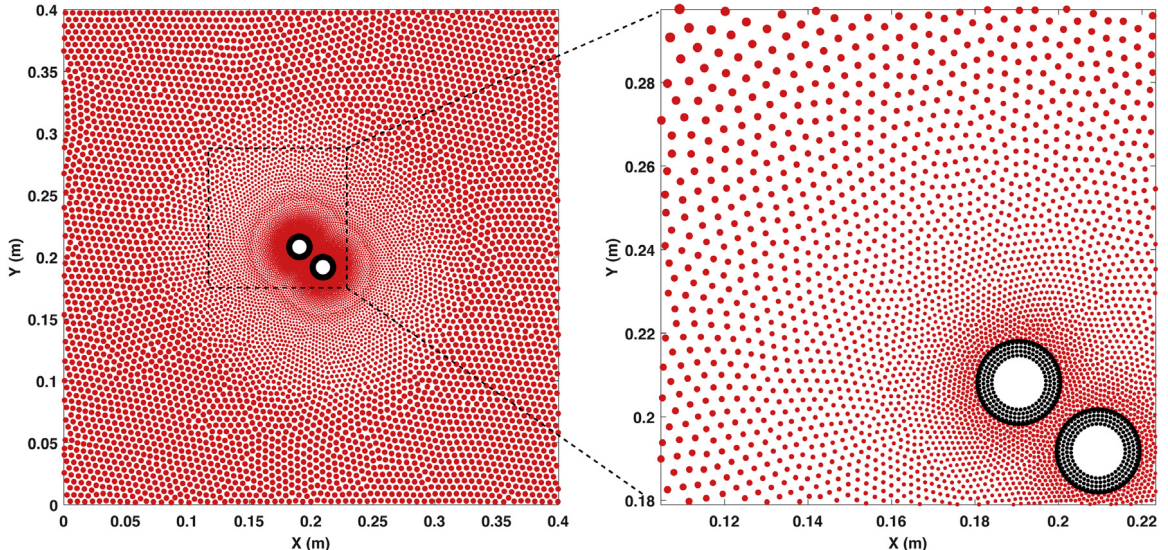


Fig. 10. A snapshot of the distribution of SPH particles around the two cylinders under a shear flow with the resolutions adapted according to the distances to the cylinders ($t = 1500$ s).

a desired distribution using the distance-based adaptive algorithm. To that end, we started with a uniform resolution $\Delta x_{ini} = 4$ mm and set $\Delta x_H = \frac{1}{4}\Delta x_{ini}$, $\gamma_{max} = \sqrt{31}$ (or $\Delta x_L = \frac{\sqrt{31}}{4}\Delta x_{ini}$), and $N_H = 400$ in Eq. (18). The adaptive algorithm was executed iteratively until the shifting vectors computed from Eq. (19) in a new iteration were sufficiently small; i.e., $\frac{1}{\beta N_{tot}} \sum_i \frac{|\delta r_i|}{\sqrt{m_i/\rho_i}} < 6 \times 10^{-3}$.

The actual simulation was “seeded” with the variable resolutions generated from the preprocessing step. We continued to use the distance-based adaptive algorithm while the two cylinders and fluid particles were moving with the flow. Fig. 10 presents a snapshot of the distribution of SPH particles with the adapted resolutions, in which the two cylinders had the initial separation of (0.03 m, 0.012 m). (The entire dynamics is shown by the animation in the Supporting Information.) As seen in Fig. 10, the resolutions were gradually coarsened away from the cylinders. With the finest resolution near the cylinders, we maintained sufficient particles to resolve the gap between the two cylinders when they approached each other closely.

Due to the symmetry of the two cylinders, we only tracked the trajectory of the left cylinder’s center of mass. Fig. 11 depicts the three trajectories computed from our simulations and compared with the analytical solutions [71].

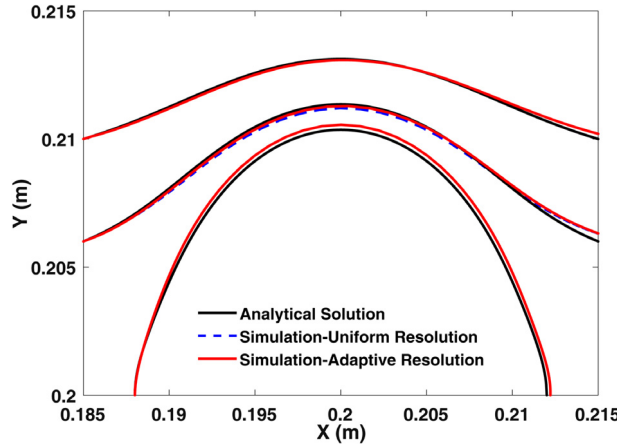


Fig. 11. Trajectories of one of the two cylinders under the shear flow with three different initial positions, computed from the consistent SPH simulations and compared with the analytical solutions [71].

Results produced by the consistent adaptive-resolution SPH satisfactorily agree with the analytical solutions. We also provide in Fig. 11 the trajectory predicted using the uniform high resolution of $\Delta x = \Delta x_H = 1$ mm, which overlaps the curve obtained from the adaptive-resolution simulation. In the case of the bottom trajectory in Fig. 11, the two cylinders could get as close as less than one particle spacing ($\Delta x_H = 1$ mm) between their boundaries. To avoid the singularity caused by lack of discretization points within the gap between the two cylinders, we followed Bian et al. [64] and applied a repulsive interaction between the cylinders based on a lubrication model [73,74] for both adaptive-resolution and uniform-resolution simulations. However, it was applied only when the two cylinders came within Δx_H between each other. Note that the number of particles used in the adaptive resolution simulation was only $\frac{1}{16}$ of that in the previous work by Bian et al., who drew on an inconsistent SPH algorithm [64]. Moreover, owing to the consistent nature of the discretization, our results show improved accuracy with better agreement with the analytical solutions. For both simulations, the time step was set as 5.0×10^{-2} s. In terms of computational efficiency, for each time step, the computational time is 0.97 s for adaptive resolution and 7.6 s for uniform-resolution. The adaptive-resolution simulation saved about 87% computer time (85% if the pre-processing step was included) compared against the simulation with the uniform high resolution.

3.5. Dynamics of an L-shaped active colloid

In this section, we reproduced an interesting phenomenon concerning the motion of an asymmetric self-propelled colloid in fluid, which was first observed in experiments [2]. The colloid is L-shaped with two asymmetric arms. The colloid's motion was constrained to 2D in the experiment [2]. Thus, we set up a 2D simulation with a domain comparable to the chamber used in the experiment [2], as depicted in Fig. 12. The no-slip BC is imposed on the surface of the L-shaped colloid; and, periodic BCs are applied at the remaining boundaries. The kinetic viscosity of the fluid was $\nu = 2.4 \times 10^{-9} \text{ m}^2/\text{s}$. Both the colloid and fluid are subject to the gravitational force \mathbf{g} with $|\mathbf{g}| = 0.3 \text{ m/s}^2$. To mimic the colloid's self-propelling mechanism as in the experiment, an effective force \mathbf{F}_e and torque \mathbf{T}_e were applied at the center of mass of the L-shaped colloid. During the motion of the colloid, the magnitude of \mathbf{F}_e was kept constant, and it is always along the longer arm of the "L" shape regardless of the orientation of the colloid. The torque \mathbf{T}_e is related to \mathbf{F}_e by $\mathbf{T}_e = (l_2 - x'_p)\mathbf{e}_{x'} \times \mathbf{F}_e$, where x'_p and $\mathbf{e}_{x'}$ are defined in the local coordinate system on the colloid. By varying the magnitude of \mathbf{F}_e , the L-shaped active colloid could display rich dynamic behavior owing to its nonlinear hydrodynamic interaction with the fluid.

As in Section 3.4, a preprocessing step preceded the actual simulation. For preprocessing, the colloid was fixed at its initial position and the spatial resolution was adapted to a desired distribution using the distance-based adaptive algorithm. To that end, we started with a uniform resolution $\Delta x_{ini} = 1 \times 10^{-6} \text{ m}$ and set $\Delta x_H = \frac{1}{2}\Delta x_{ini}$, $\Delta x_L = \frac{\sqrt{7}}{2}\Delta x_{ini}$ (i.e., $\Upsilon_{max} = \sqrt{7}$), and $N_H = 700$. Iterations of the adaptive algorithm ended when the shifting vectors computed from Eq. (19) satisfied $\frac{1}{\beta N_{tot}} \sum_i \frac{|\delta \mathbf{r}_i|}{\sqrt{m_i/\rho_i}} < 6 \times 10^{-3}$. The actual experiment commenced after this

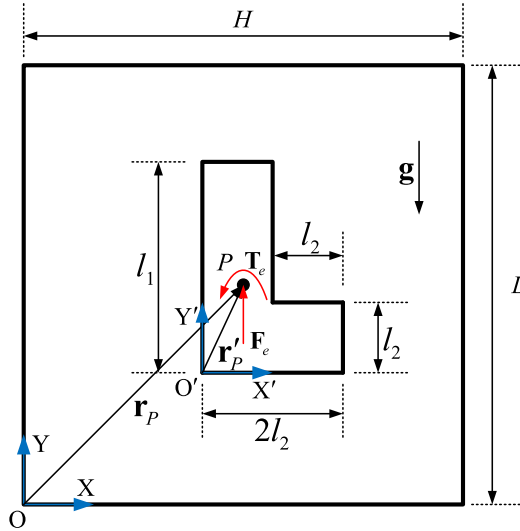


Fig. 12. Configuration of the simulation domain and L-shaped colloid. Here, $H = L = 100 \times 10^{-6}$ m; $l_1 = 18 \times 10^{-6}$ m; and, $l_2 = 6 \times 10^{-6}$ m. The coordinates of the center of mass of the colloid are $(x'_p, y'_p) = (4.5 \times 10^{-6}$ m, 7.5×10^{-6} m), with the origin O' of the local coordinate system set at the bottom left corner of the “L” shape. \mathbf{F}_e and \mathbf{T}_e represent the effective force and torque acting on the colloid to induce its self-propulsion.

preprocessing step. During the simulation, the error-based adaptive algorithm was employed to dynamically adapt spatial resolutions while the colloid and fluid particles were moving with the flow. Fig. 13 presents two snapshots of the simulation, showing the distributions of adaptive resolutions around the L-shaped colloid and throughout the domain at two different time instances. (The entire dynamics is shown by the animation in the Supporting Information.)

As observed in the experiment [2], with the magnitude of \mathbf{F}_e varied, the L-shaped active colloid followed different trajectories. For a small \mathbf{F}_e , the colloid’s self-propelling motion was slow. As a result, the impact of gravitational force was dominant, and hence, the colloid did a straight downward swimming (SDS). As \mathbf{F}_e gradually increased, the active motion of the colloid sped up, and its hydrodynamic interaction with the fluid started to compete with the impact of gravitational force and produced a trochoid-like motion (TLM) or even straight upward swimming (SUS). Our simulations were able to predict these three motions of the colloid. As illustrated in Fig. 14, the trajectories of the colloid at four different magnitudes of \mathbf{F}_e display its SDS, TLM, and SUS motions. For the most complicated TLM, we further compared the trochoid-like trajectory predicted by the adaptive-resolution simulation with that computed from the uniform high-resolution ($\Delta x = \Delta x_H = 0.5 \times 10^{-6}$ m) simulation. A good agreement is found in the two solutions. Meanwhile, the adaptive-resolution simulation only used $\frac{1}{4}$ of SPH particles needed in the uniform high-resolution simulation and was two times faster in terms of computer time than the uniform high-resolution simulation. For both simulations, the time step was set as 5.0×10^{-3} s. For each time step, the computational time is 0.85 s for adaptive resolution and 1.95 s for uniform-resolution.

3.6. Collective dynamics of active colloids

Lastly, we simulated a more challenging problem — the collective dynamics of a suspension of colloids. The colloids were actively rotating with a constant speed. As discussed in the literature [3], these active colloids were driven by hydrodynamic interactions to repel or attract each other and hence could display rich collective behaviors. The simulation domain is 0.36 m by $0.24\sqrt{3}$ m. Initially, 48 equal-sized circular disks with a radius of $R_d = 0.0125$ m were randomly placed in the domain. Each disk rotated clockwise with the same prescribed angular velocity of $\omega_d = 10^{-2}$ rad/s. The kinetic viscosity of the fluid was $\nu = 0.263 \times 10^{-6}$ m²/s. This problem setup yields an area fraction of 0.04 for the colloid suspension and a Reynolds number (defined as $Re = \frac{\omega_d R_d^2}{\nu}$) of 5.94, which match those considered in the literature [3]. The flow was subject to no-slip BC at the surfaces of colloids and periodic BCs at the remaining boundaries. The spatial resolutions were adapted according to the recovery-based error estimator.

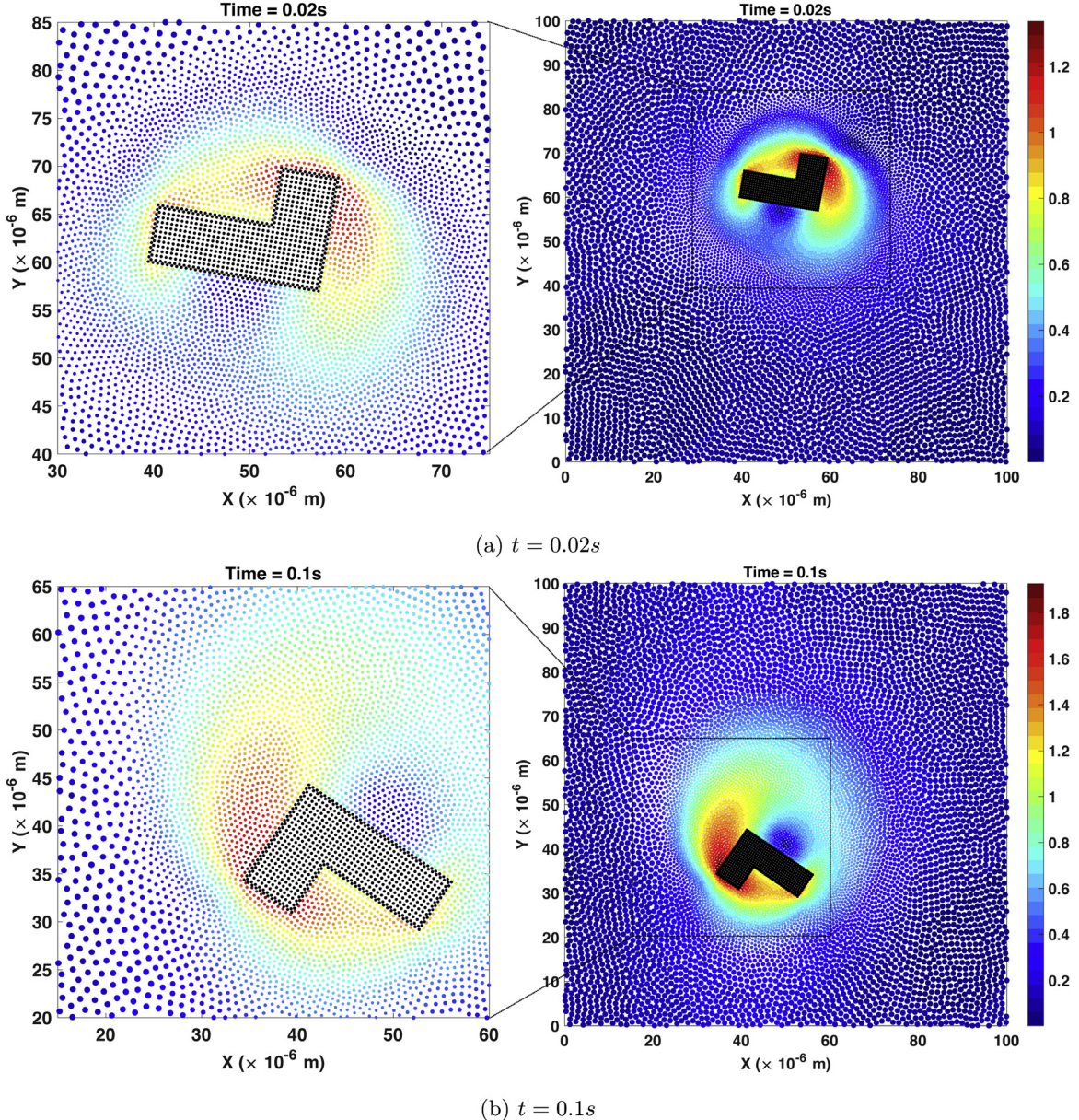


Fig. 13. Two snapshots of the distribution of SPH particles around the L-shaped colloid at $t = 0.02, 0.1$ s. The color is correlated to the flow velocity magnitude (unit in the color bar: 10^{-3} m/s). (For interpretation of the references to color in this figure legend, the reader is referred to the web version of this article.)

Initially, the SPH fluid particles were distributed with a uniform spacing $\Delta x_{ini} = 4$ mm. The finest resolution was prescribed as $\Delta x_H = \frac{1}{2}\Delta x_{ini}$; and, the maximum resolution ratio was $\Upsilon_{max} = \sqrt{7}$.

According to the work by Goto [3], the collective behavior of these active disks depend on the Reynolds number. At $Re = 5.94$, the colloids finally formed a stable hexagonal, ordered crystal-like configuration. We reproduced this observation in our simulation. Fig. 15 presents a snapshot of the colloids in this simulation, from which the hexagonal, ordered configuration can be clearly observed. Once this ordered configuration was formed, it remained stable throughout the entire simulation. When Re was increased to 15.625, the system became unstable. The colloids moved around each other but could not form any ordered configuration, same as reported by Goto [3]. Fig. 16 shows a

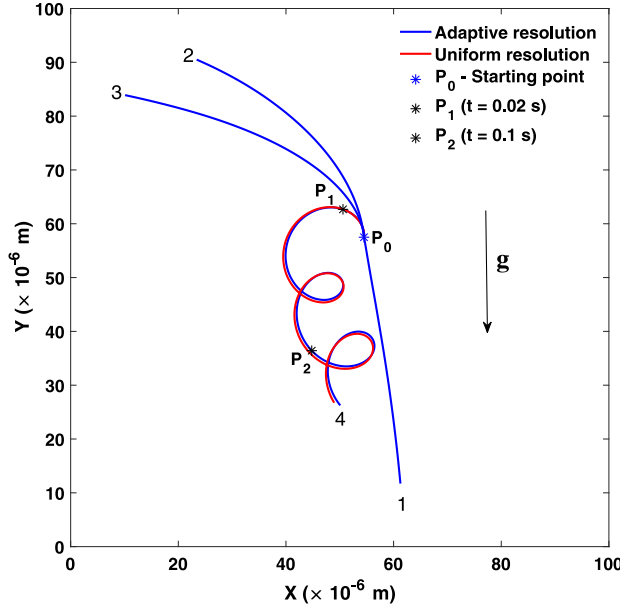


Fig. 14. Trajectories of the L-shaped colloid at four different magnitudes of \mathbf{F}_e . All trajectories start at the same position (blue asterisk). Trajectory 1 corresponds to the SDS with $|\mathbf{F}_e| = 0.06 \text{ m/s}^2$; trajectories 2 and 3 correspond to the SUS with $|\mathbf{F}_e| = 0.45, 0.6 \text{ m/s}^2$, respectively; and, trajectory 4 corresponds to the TLM with $|\mathbf{F}_e| = 1.2 \text{ m/s}^2$. The two marked points (black asterisk) correspond to the two snapshots shown in Fig. 13 at $t = 0.02, 0.1 \text{ s}$, respectively . (For interpretation of the references to color in this figure legend, the reader is referred to the web version of this article.)

snapshot from the simulation with $Re = 15.625$, in which the colloids are randomly distributed even after a long time simulation. In Figs. 15 and 16, we note that the error-based criterion gave rise to finer resolutions near the colloids' boundaries, which led to more accurate solutions for the near-field hydrodynamic interactions between colloids.

4. Conclusion

We have presented a new adaptive-resolution SPH method. It accurately captures the near-field hydrodynamic variables in FSI with sufficiently high resolutions and enlarges the computational capability of FSI problems without increasing the computational cost.

A three-step adaptive algorithm was proposed to dynamically adapt spatial resolutions during the simulation. A key element of this algorithm is the criterion of adaptivity, of which we assessed two. The first one is distance-based, in which the spatial resolutions in the fluid domain gradually vary according to the distances to the solid boundary. The second criterion is error-based and adapts the resolutions according to a *a posteriori* recovery-based error estimator and following the error equidistribution strategy. In practice, these two criteria can be combined to optimize the accuracy and efficiency of the numerical simulations. As demonstrated in one of the tests (Section 3.5), the distance-based criterion was employed in preprocessing to generate an initial distribution of adaptive resolutions. The error-based criterion was subsequently used in the simulation for dynamically adapting resolutions.

A noteworthy component of the adaptive algorithm is its particle-shifting technique employed for refining or coarsening resolutions. In the proposed approach, the SPH particles marked for refinement/coarsening had their masses changed first while the total mass of particles was conserved. Thereafter, shifting vectors were computed for positioning the particles at their new locations. Subsequently, the hydrodynamic variables were corrected using second-order interpolation to account for their new positions.

We applied the new method in simulating six different flow and FSI problems: the transient Poiseuille flow, flow around a periodic array of cylinders, flow around a cylinder in a narrow channel, two colloids rotating under a shear flow, dynamics of a L-shaped active colloid, and collective dynamics of a suspension of active colloids. The numerical results were compared with analytical predictions, experimental data, and simulation results from FEM or the consistent SPH with a uniform, high resolution. For all tests we noted good accuracy, second-order

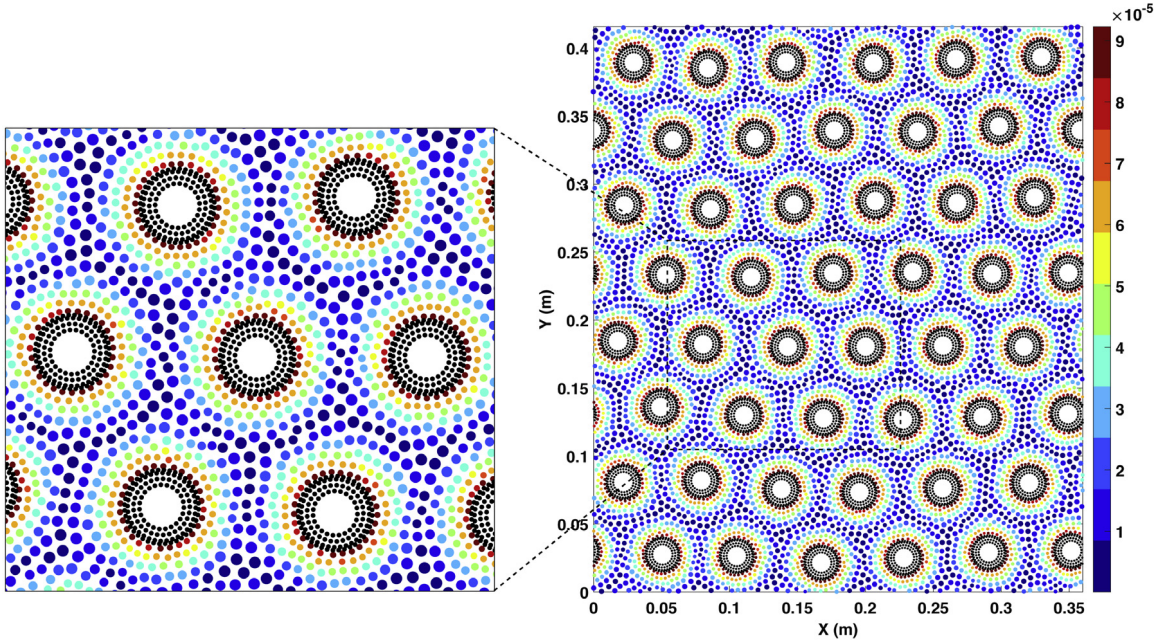


Fig. 15. A suspension of active colloids with a hexagonal-ordered configuration at $Re = 5.94$. The spatial resolutions were adapted according to the recovery-based error computed during the simulation. The color is correlated to the flow velocity magnitude (unit in the color bar: m/s). (For interpretation of the references to color in this figure legend, the reader is referred to the web version of this article.)

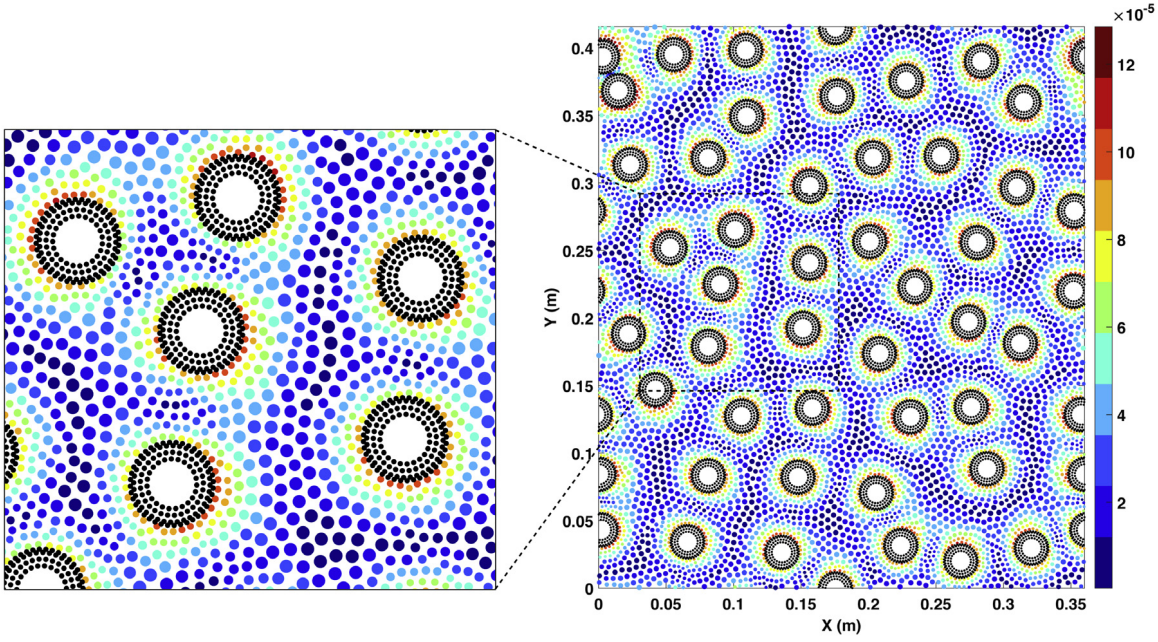


Fig. 16. A suspension of active colloids randomly distributed at $Re = 15.625$. The spatial resolutions were adapted according to the recovery-based error computed during the simulation. The color is correlated to the flow velocity magnitude (unit in the color bar: m/s). (For interpretation of the references to color in this figure legend, the reader is referred to the web version of this article.)

convergence, and significant reductions in SPH particle counts and computer time. The method was found flexible and robust in modeling various FSI problems with stationary or moving (translating and rotating) boundaries of arbitrary geometries. Although the simulations were conducted in 2D, the proposed method is directly applicable to

a 3D implementation, which insofar efficiency gains are concerned, stands to benefit even more from the proposed adaptive-resolution approach.

The second-order consistent discretization of differential operators was employed in this work. In the adaptive-resolution scenario, this discretization ensures consistency in the discretization of the gradient and Laplacian operators even when SPH particles of different sizes (variable resolutions) are coupled within a kernel support. However, we note that the overall accuracy of the numerical solution for the Navier–Stokes equations also depends on how the pressure is approximated. In this work, the weakly compressible equation of state was employed to approximate incompressibility and to solve for the pressure, which is not numerically consistent. In addition, the formulation in Eq. (12) used for evaluating the pressure force exerted on the solid body is not compatible with the consistent discretization. Thus, if the pressure force significantly comes into play in FSI, the second-order accuracy cannot be guaranteed in the numerical solutions. In our future work, we will enforce the incompressibility using the second-order projection method, as in our previous work [41], and employ a formula compatible with the consistent discretization for calculating the pressure-force, as in [75], to further improve the accuracy of the proposed adaptive-resolution SPH method for FSI simulations.

Acknowledgments

W.P. acknowledges partial support from Pacific Northwest National Laboratory (PNNL) USA under Subcontract 384038. PNNL is operated by Battelle for DOE under Contract DE-AC05-76RL01830.

Appendix A. Supplementary data

Supplementary material related to this article can be found online at <https://doi.org/10.1016/j.cma.2018.10.049>.

References

- [1] J. Bueno, C. Bona-Casas, Y. Bazilevs, H. Gomez, Interaction of complex fluids and solids: theory, algorithms and application to phase-change-driven implosion, *Comput. Mech.* 55 (6) (2015) 1105–1118.
- [2] B. Ten Hagen, F. Kümmerl, R. Wittkowski, D. Takagi, H. Löwen, C. Bechinger, Gravitaxis of asymmetric self-propelled colloidal particles, *Nature Commun.* 5 (2014) 4829.
- [3] Y. Goto, H. Tanaka, Purely hydrodynamic ordering of rotating disks at a finite Reynolds number, *Nature Commun.* 6 (2015) 1–10.
- [4] A. Randles, D.H. Frakes, J.A. Leopold, Computational fluid dynamics and additive manufacturing to diagnose and treat cardiovascular disease, *Trends Biotechnol.* 35 (11) (2017) 1049–1061.
- [5] T. Kamps, M. Biedermann, C. Seidel, G. Reinhart, Design approach for additive manufacturing employing constructal theory for point-to-circle flows, *Addit. Manuf.* 20 (2018) 111–118.
- [6] R.D. Sochol, E. Sweet, C.C. Glick, S. Venkatesh, A. Avetisyan, K.F. Ekman, A. Raulinaitis, A. Tsai, A. Wienkers, K. Korner, et al., 3D printed microfluidic circuitry via multijet-based additive manufacturing, *Lab Chip* 16 (4) (2016) 668–678.
- [7] S. Sarmad, J.-P. Mikkola, X. Ji, Carbon dioxide capture with ionic liquids and deep eutectic solvents: a new generation of sorbents, *ChemSusChem* 10 (2) (2017) 324–352.
- [8] A. Tagiuri, K.Z. Sumon, A. Henni, K. Zanganeh, A. Shafeen, Effect of cation on the solubility of carbon dioxide in three bis (fluorosulfonyl) imide low viscosity ([fsi]) ionic liquids, *Fluid Phase Equilib.* 375 (2014) 324–331.
- [9] D.Y. Leung, G. Caramanna, M.M. Maroto-Valer, An overview of current status of carbon dioxide capture and storage technologies, *Renew. Sustain. Energy Rev.* 39 (2014) 426–443.
- [10] J.J. Monaghan, Smoothed particle hydrodynamics, *Rep. Progr. Phys.* 68 (2005) 1703–1759.
- [11] R. Fatehi, M. Manzari, Error estimation in smoothed particle hydrodynamics and a new scheme for second derivatives, *Comput. Math. Appl.* 61 (2011) 482–498.
- [12] G. Oger, M. Doring, B. Alessandrini, P. Ferrant, An improved sph method: towards higher order convergence, *J. Comput. Phys.* 225 (2) (2007) 1472–1492.
- [13] S. Adam, X. Hu, N. Adams, A new surface-tension formulation for multi-phase sph using a reproducing divergence approximation, *J. Comput. Phys.* 229 (13) (2010) 5011–5021.
- [14] N. Tofighi, M. Yildiz, Numerical simulation of single droplet dynamics in three-phase flows using isph, *Comput. Math. Appl.* 66 (4) (2013) 525–536.
- [15] A.M. Tartakovsky, A. Panchenko, Pairwise force smoothed particle hydrodynamics model for multiphase flow: surface tension and contact line dynamics, *J. Comput. Phys.* 305 (2016) 1119–1146.
- [16] W. Pan, A.M. Tartakovsky, J.J. Monaghan, Smoothed particle hydrodynamics model for ice sheet and ice shelf dynamics, *J. Glaciol.* 58 (2012) 216–222.
- [17] W. Pan, A.M. Tartakovsky, J.J. Monaghan, Smoothed particle hydrodynamics non-newtonian model for ice sheet and ice shelf dynamics, *J. Comput. Phys.* 242 (2013) 828–842.

- [18] X. Xua, P. Yu, A multiscale sph method for simulating transient viscoelastic flows using bead-spring chain model, *J. Non-Newton. Fluid Mech.* 229 (2016) 27–42.
- [19] A. Vázquez-Quesada, M. Ellero, Rheology and microstructure of non-colloidal suspensions under shear studied with smoothed particle hydrodynamics, *J. Non-Newton. Fluid Mech.* 233 (2016) 37–47.
- [20] J. Gray, J. Monaghan, R. Swift, Sph elastic dynamics, *Comput. Methods Appl. Mech. Engrg.* 190 (49) (2001) 6641–6662.
- [21] W. Pan, D. Li, A.M. Tartakovsky, S. Ahzi, M. Khraisheh, M. Khaleel, A new smoothed particle hydrodynamics non-newtonian model for friction stir welding: process modeling and simulation of microstructure evolution in a magnesium alloy, *Int. J. Plast.* 48 (2013) 189–204.
- [22] W. Hu, Q. Tian, H. Hu, Dynamic fracture simulation of flexible multibody systems via coupled finite elements of ancf and particles of SPH, *Nonlinear Dynam.* 84 (4) (2016) 2447–2465.
- [23] W. Hu, Q. Tian, H. Hu, Dynamic simulation of liquid-filled flexible multibody systems via absolute nodal coordinate formulation and sph method, *Nonlinear Dynam.* 75 (4) (2014) 653–671.
- [24] M. Schörgenhofer, P.G. Gruber, J. Gerstmayer, Interaction of flexible multibody systems with fluids analyzed by means of smoothed particle hydrodynamics, *Multibody Syst. Dyn.* 30 (1) (2013) 53–76.
- [25] A. Pazouki, R. Serban, D. Negrut, A high performance computing approach to the simulation of fluid-solid interaction problems with rigid and flexible components, *Arch. Mech. Eng.* 61 (2) (2014) 227–251.
- [26] J. Kordilla, W. Pan, A. Tartakovsky, Smoothed particle hydrodynamics model for landau-lifshitz-navier-stokes and advection-diffusion equations, *J. Chem. Phys.* 141 (22) (2014) 224112.
- [27] A.M. Tartakovsky, N. Trask, K. Pan, B. Jones, W. Pan, J.R. Williams, Smoothed particle hydrodynamics and its applications for multiphase flow and reactive transport in porous media, *Comput. Geosci.* 20 (4) (2016) 807–834.
- [28] W. Pan, M. Daily, N.A. Baker, Numerical calculation of protein-ligand binding rates through solution of the smoluchowski equation using smoothed particle hydrodynamics, *BMC Biophys.* 8 (2015) 7–18.
- [29] S. Liu, J. Savage, G.A. Voth, Mesoscale study of proton transport in proton exchange membranes: role of Morphology, *J. Phys. Chem. C* 119 (4) (2015) 1753–1762.
- [30] M. Lastiwka, M. Basa, N.J. Quinlan, Permeable and non-reflecting boundary conditions in SPH, *Internat. J. Numer. Methods Fluids* 61 (7) (2009) 709–724.
- [31] G. Oger, M. Doring, B. Alessandrini, P. Ferrant, Two-dimensional sph simulations of wedge water entries, *J. Comput. Phys.* 213 (2) (2006) 803–822.
- [32] J. Feldman, J. Bonet, Dynamic refinement and boundary contact forces in sph with applications in fluid flow problems, *Internat. J. Numer. Methods Engrg.* 72 (3) (2007) 295–324.
- [33] Y. Reyes López, D. Roose, C. Recarey Morfa, Dynamic particle refinement in sph: Application to free surface flow and non-cohesive soil simulations, *Comput. Mech.* 51 (5) (2013) 731–741.
- [34] R. Vacondio, B.D. Rogers, P.K. Stansby, P. Mignosa, J. Feldman, Variable resolution for sph: A dynamic particle coalescing and splitting scheme, *Comput. Methods Appl. Mech. Engrg.* 256 (2013) 132–148.
- [35] D.A. Barcarolo, D. Le Touzé, G. Oger, F. De Vuyst, Adaptive particle refinement and derefinement applied to the smoothed particle hydrodynamics method, *J. Comput. Phys.* 273 (2014) 640–657.
- [36] X. Bian, Z. Li, G.E. Karniadakis, Multi-resolution flow simulations by smoothed particle hydrodynamics via domain decomposition, *J. Comput. Phys.* 297 (2015) 132–155.
- [37] R. Vacondio, B. Rogers, P. Stansby, P. Mignosa, Variable resolution for sph in three dimensions: Towards optimal splitting and coalescing for dynamic adaptivity, *Comput. Methods Appl. Mech. Engrg.* 300 (2016) 442–460.
- [38] W. Hu, W. Pan, M. Rakhsa, Q. Tian, H. Hu, D. Negrut, A consistent multi-resolution smoothed particle hydrodynamics method, *Comput. Methods Appl. Mech. Engrg.* 324 (2017) 278–299.
- [39] P. Omidvar, P.K. Stansby, B.D. Rogers, Wave body interaction in 2d using smoothed particle hydrodynamics (SPH) with variable particle mass, *Internat. J. Numer. Methods Fluids* 68 (6) (2012) 686–705.
- [40] N. Trask, M. Maxey, K. Kimb, M. Perego, M.L. Parks, K. Yang, J. Xu, A scalable consistent second-order sph solver for unsteady low Reynolds number flows, *Comput. Methods Appl. Mech. Engrg.* 289 (2015) 155–178.
- [41] W. Pan, K. Kim, M. Perego, A.M. Tartakovsky, M.L. Parks, Modeling electrokinetic flows by consistent implicit incompressible smoothed particle hydrodynamics, *J. Comput. Phys.* 334 (2017) 125–144.
- [42] Z. Meglicki, D. Wickramasinghe, G.V. Bicknell, 3D structure of truncated accretion discs in close binaries, *Mon. Not. R. Astron. Soc.* 264 (3) (1993) 691–704.
- [43] S. Kitsionas, A.P. Whitworth, Smoothed particle hydrodynamics with particle splitting, applied to self-gravitating collapse, *Mon. Not. R. Astron. Soc.* 330 (1) (2002) 129–136.
- [44] S. Kitsionas, A.P. Whitworth, High-resolution simulations of clump–clump collisions using sph with particle splitting, *Mon. Not. R. Astron. Soc.* 378 (2) (2007) 507–524.
- [45] R. Vacondio, B. Rogers, P. Stansby, Accurate particle splitting for smoothed particle hydrodynamics in shallow water with shock capturing, *Internat. J. Numer. Methods Fluids* 69 (8) (2012) 1377–1410.
- [46] P.R. Shapiro, H. Martel, J.V. Villumsen, J.M. Owen, Adaptive smoothed particle hydrodynamics, with application to cosmology: methodology, *Astrophys. J. Suppl. Ser.* 103 (1996) 269.
- [47] J.M. Owen, J.V. Villumsen, P.R. Shapiro, H. Martel, Adaptive smoothed particle hydrodynamics: methodology. II., *Astrophys. J. Suppl. Ser.* 116 (2) (1998) 155.
- [48] M. Liu, G. Liu, Meshfree particle simulation of micro channel flows with surface tension, *Comput. Mech.* 35 (5) (2005) 332–341.
- [49] M. Liu, G. Liu, K. Lam, Adaptive smoothed particle hydrodynamics for high strain hydrodynamics with material strength, *Shock Waves* 15 (1) (2006) 21–29.

- [50] R. Verfürth, A Review of a Posteriori Error Estimation and Adaptive Mesh-refinement Techniques, John Wiley & Sons Inc, 1996.
- [51] R.H. Nochetto, K.G. Siebert, A. Veeser, Theory of adaptive finite element methods: an introduction, in: Multiscale, Nonlinear and Adaptive Approximation, Springer, Berlin, 2009, pp. 409–542.
- [52] O. Zienkiewicz, J. Zhu, The superconvergent patch recovery (spr) and adaptive finite element refinement, *Comput. Methods Appl. Mech. Engrg.* 101 (1) (1992) 207–224.
- [53] M. Ainsworth, J.T. Oden, A Posteriori Error Estimation in Finite Element Analysis, John Wiley & Sons, Inc., 2000, pp. 65–84.
- [54] J. Xu, Z. Zhang, Analysis of recovery type a posteriori error estimators for mildly structured grids, *Math. Comp.* 73 (247) (2004) 1139–1152 (electronic).
- [55] Z. Zhang, A. Naga, A new finite element gradient recovery method: superconvergence Property, *SIAM J. Sci. Comput.* 26 (4) (2005) 1192–1213.
- [56] A. Naga, Z. Zhang, A posteriori error estimates based on the polynomial preserving recovery, *SIAM J. Numer. Anal.* 42 (4) (2004) 1780–1800.
- [57] H. Takeda, S.M. Miyama, M. Sekiya, Numerical simulation of viscous flow by smoothed particle hydrodynamics, *Progr. Theoret. Phys.* 92 (5) (1994) 939–960.
- [58] J.P. Morris, P.J. Fox, Y. Zhu, Modeling low reynolds number incompressible flows using SPH, *J. Comput. Phys.* 136 (1) (1997) 214–226.
- [59] F. Maciá, M. Antuono, L. Gonzalez, A. Colagrossi, Theoretical analysis of the no-slip boundary condition enforcement in sph methods, *Progr. Theoret. Phys.* 125 (6) (2011) 1091–1121.
- [60] D.W. Holmes, J.R. Williams, P. Tilke, Smooth particle hydrodynamics simulations of low reynolds number flows through porous media, *Int. J. Numer. Anal. Methods Geomech.* 35 (4) (2011) 419–437.
- [61] J.P. Morris, Simulating surface tension with smoothed particle hydrodynamics, *Int. J. Numer. Methods Fluids* 33 (3) (2000) 333–353.
- [62] M. Antuono, A. Colagrossi, S. Marrone, D. Molteni, Free-surface flows solved by means of sph schemes with numerical diffusive terms, *Comput. Phys. Comm.* 181 (3) (2010) 532–549.
- [63] S. Marrone, A. Di Mascio, D. Le Touzé, Coupling of smoothed particle hydrodynamics with finite volume method for free-surface flows, *J. Comput. Phys.* 310 (2016) 161–180.
- [64] X. Bian, M. Ellero, A splitting integration scheme for the sph simulation of concentrated particle suspensions, *Comput. Phys. Comm.* 185 (1) (2014) 53–62.
- [65] S. Adami, X. Hu, N. Adams, A generalized wall boundary condition for smoothed particle hydrodynamics, *J. Comput. Phys.* 231 (21) (2012) 7057–7075.
- [66] J. Monaghan, On the problem of penetration in particle methods, *J. Comput. Phys.* 82 (1) (1989) 1–15.
- [67] J.J. Monaghan, Simulating free surface flows with SPH, *J. Comput. Phys.* 110 (2) (1994) 399–406.
- [68] J.J. Monaghan, Smoothed particle hydrodynamics, *Annu. Rev. Astron. Astrophys.* 30 (1) (1992) 543–574.
- [69] R. Xu, P. Stansby, D. Laurence, Accuracy and stability in incompressible sph (ISPH) based on the projection method and a new approach, *J. Comput. Phys.* 228 (18) (2009) 6703–6725.
- [70] J.-T. Jeong, S.-H. Yoon, Two-dimensional stokes flow around a circular cylinder in a microchannel, *J. Mech. Sci. Technol.* 28 (2) (2014) 573–579.
- [71] C. Darabanel, J. Raasch, S. Mason, Particle motions in sheared suspensions xx: circular cylinders, *Can. J. Chem. Eng.* 45 (1) (1967) 3–12.
- [72] N. Trask, M. Maxey, X. Hu, A compatible high-order meshless method for the stokes equations with applications to suspension flows, *J. Comput. Phys.* 355 (2018) 310–326.
- [73] X. Yuan, R. Ball, Rheology of hydrodynamically interacting concentrated hard disks, *J. Chem. Phys.* 101 (10) (1994) 9016–9021.
- [74] J. Kromkamp, D. van den Ende, D. Kandhai, R. van der Sman, R. Boom, Lattice Boltzmann simulation of 2D and 3D non-Brownian suspensions in Couette flow, *Chem. Eng. Sci.* 61 (2) (2006) 858–873.
- [75] M. Hashemi, R. Fatehi, M. Manzari, A modified sph method for simulating motion of rigid bodies in newtonian fluid flows, *Int. J. Non-Linear Mech.* 47 (6) (2012) 626–638.